



Synthesis of acidic MIL-125 from plastic waste: Significant contribution of N orbital for efficient photocatalytic degradation of chlorobenzene and toluene

Xiaodong Zhang^{a,*}, Ke Yue^a, Renzhi Rao^a, Jinfeng Chen^a, Qiang Liu^a, Yang Yang^a, Fukun Bi^a, Yuxin Wang^b, Jingcheng Xu^c, Ning Liu^{a,*}

^a School of Environment and Architecture, University of Shanghai for Science and Technology, Shanghai 200093, China

^b Institute of Applied Biotechnology, Taizhou Vocation & Technical College, Taizhou, Zhejiang 318000, China

^c School of Materials and Chemistry, University of Shanghai for Science and Technology, Shanghai 200093, China

ARTICLE INFO

Keywords:

Plastic
Photocatalysis
Functional group modification
Degradation pathways
Chlorobenzene

ABSTRACT

Development of efficient and stable catalyst for the degradation of chlorinated volatile organic compounds (VOCs) is a hot research topic. In this study, we used plastic-based terephthalic acid for the synthesis of MIL-125, which further modified by the -NH₂ and -NO₂ groups. DFT calculations revealed that the N orbitals had an important contribution in reducing the band gap, leading to easier hydrogen absorption and high electron transfer efficiency. Optical studies, XPS, TRES, NH₃-TPD and pyridine IR further demonstrated that the amino modification promoted the visible absorption range and acidity of MIL-125 in comparison to the nitro modification, resulting in efficient catalytic degradation of chlorobenzene and toluene, even in the presence of water. This work provides an economically feasible strategy for modifying metal organic frameworks (MOFs) and suggests the possible VOCs degradation pathways with EPR, in situ FTIR, GC-MS and TG-MS analysis.

1. Introduction

The large amount of chlorinated volatile organic compounds VOCs emitted by chemical industries has led to serious environmental problems, such as the formation of urban photochemical smog and the depletion of the ozone layer in the troposphere. Chlorobenzene and toluene are typical harmful pollutants and have caused significant damage to the environment and human health [1]. Among these, chlorobenzene is environmentally stable and not easily removed owing to its resistance against biodegradation, which subsequently leads to its bioaccumulation [2]. Photocatalysis, which requires low energy consumption and is a sustainable and clean process, can degrade chlorobenzene and toluene [3]. Catalysts with acidic surfaces have been reported to readily adsorb organic reactants, thereby promoting their photocatalytic decomposition [4]. However, the development of efficient photocatalysts with an acidic surface remain challenging. Metal organic frameworks (MOFs) are porous materials formed by the self-assembly of metal ions with organic ligands [5], and have a pore size, modifiable structure, and high specific surface area, which can be utilized in many fields such as photocatalysis [3], adsorption [6,7],

catalysis [8,9]. The synthesis of most MOFs requires the use of precious metals and expensive ligands as raw materials, and consequently, the high synthesis cost of MOFs limits their applications. Therefore, the preparation of low-cost MOFs for large-scale production and application remains challenging. Joshi et al. reported that the price of 1 kg of MIL-53 (Al) made from waste plastic bottles and waste aluminum foil was one-third of the price of the same MOF prepared from the same material provided by Sigma Aldrich and Basolite A100 [10]. Plastic-based terephthalic acid (P-H₂BDC) obtained from plastic bottles meets the requirements for the preparation of MOFs and is inexpensive and easily recyclable from the resource [11–13]. Moreover, the synthesized MOFs can be purified using the solvent density discrimination method [14]. Therefore, it is economically feasible to extract useful ligands from useless and accessible waste materials and convert them into high-quality MOFs in high yield.

Among the various types of MOFs, titanium-based MOF (MIL-125) is a common photocatalyst with tetravalent Ti⁴⁺ cations, strong redox ability and visible-light response [15]. However, the low photocatalytic activity of MIL-125 severely limits its application in photocatalysis. Some strategies had been adopted to improve the performance of

* Corresponding authors.

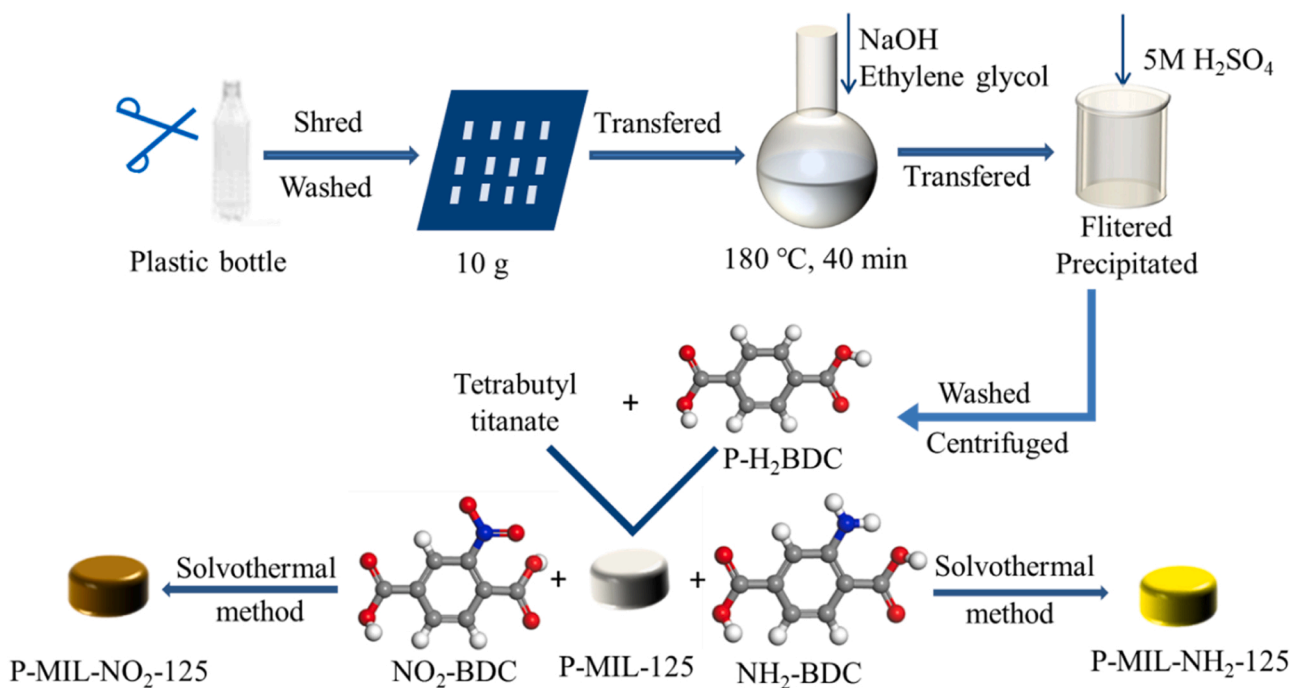
E-mail addresses: fatzhxd@126.com (X. Zhang), liuning6910@163.com (N. Liu).

<https://doi.org/10.1016/j.apcatb.2022.121300>

Received 31 October 2021; Received in revised form 5 March 2022; Accepted 8 March 2022

Available online 11 March 2022

0926-3373/© 2022 Elsevier B.V. All rights reserved.



Scheme 1. Schematic illustration for the synthesis of terephthalic acid and MIL-125 samples.

various aspects of MIL-125 (Ti), which could be divided into photo-sensitization modification, functional group modification, structural defect design, metal ion doping, heterostructure construction, and calcination to generate derivatives [3]. Modification of organic ligands was a typical method used to improve the photocatalytic activity of MOF materials at the molecular level, which could increase the light response range of the ligand and change the bandgap energy of MOF materials to a certain extent. In 2012, Li et al. prepared NH₂-MIL-125 for the first time through amino modification [16]. The light absorption ability wavelength of NH₂-MIL-125 was better than that of MIL-125 at 350 nm light absorption ability. NH₂-MIL-125 had a stable octahedral structure, and the absorption wavelength reached 550 nm. Huang et al. achieved the photocatalytic nitrogen fixation from N₂ to NH₃ by synthesizing several MIL-125 samples with simple substitution ligands [17]. Due to the linkage of the Ti site to the amino group, amino-functionalized MIL-125 showed the higher photocatalytic efficiency in comparison to OH-MIL-125. Therefore, functional group modification of MOFs is an efficient strategy for improving the photocatalytic degradation of VOCs by MOFs.

In this work, firstly, plastic fragments were used to depolymerized to H₂BDC, and then this ligand was used to synthesize functional group-modified MIL-125 by post-treatment for the efficient degradation of toluene and chlorobenzene. It was found that MOFs could degrade VOCs rapidly, especially CVOs. Secondly, the effect of N from different ligand used on photocatalytic chlorobenzene and toluene performances had been thoroughly studied using a series of characterization techniques and DFT calculations. The results combined with NH₃-TPD and pyridine IR, P-NH₂-MIL-125 synthesized using P-H₂BDC had more Lewis acidic sites to rapidly adsorb toluene and chlorobenzene. Finally, possible photocatalytic reaction pathways, especially for chlorobenzene were deduced based on the results of in situ FTIR, GC-MS, TG-MS and EPR, providing insight into the degradation pathways compared with previous literature.

2. Experimental

Details of materials and catalyst characterization are provided in detail in the [Supporting Information](#). The characterization techniques

are studied including X-ray diffractometer (XRD), fourier transform infrared FTIR spectroscopy, scanning electronic microscopy (SEM), transmission electron microscope (TEM), UV-Vis diffuse reflectance spectra (UV-vis DRS), Brunauer-Emmett-Teller (BET) analysis, X-ray photoelectron spectroscopy (XPS), photoluminescence (PL) spectroscopy, Time-resolved emission spectra (TRES), temperature-programmed desorption of ammonia (NH₃-TPD), pyridine IR spectroscopy, electron paramagnetic resonance (EPR) spectroscopy, in situ FTIR spectroscopy, gas chromatography-mass spectrometry (GC-MS) and thermogravimetric mass spectrometry (TG-MS).

2.1. Catalyst preparation

2.1.1. Synthesis of terephthalic acid from plastic bottles

Plastic was depolymerized by the acidic and alkaline hydrolysis of PET flakes. A schematic of P-H₂BDC synthesis is provided in [Scheme 1](#). First, the plastic waste bottles were cut into pieces of suitable sizes and washed with deionized water and anhydrous ethanol. Subsequently, 12 g of NaOH, 55 mL of ethylene glycol and 10 g of PET flakes were added to a round-bottom flask attached to a reflux condenser and heated to 180 °C for 40 min. During this process, the plastic gradually decomposed and the solution turned milky white. After the completion of this process, the round-bottom flask was removed from the magnetic stirrer and cooled to room temperature. Subsequently, 300 mL of deionized water was added to the flask while stirring. The resulting solution was filtered using a filter paper to remove the undecomposed particles. The filtered solution was stirred vigorously. Sulfuric acid (5 mol/L) was added dropwise while stirring to form a white precipitate and the solution was left for 30 min. The white precipitate was separated by centrifugation and washed four times with deionized water. Finally, the centrifuged product was dried at 100 °C for 12 h to obtain P-H₂BDC (7 g) as a white solid. The FT-IR characterization ([Fig. S1a](#)) of P-H₂BDC was consistent with that reported in the literature [18].

2.1.2. Synthesis of catalysts

First, MIL-125 was synthesized using a literature method after some modification [17]. Commercial H₂BDC (1 g) was then added to the mixture of DMF (18 mL) and MeOH (2 mL). The solution was sonicated

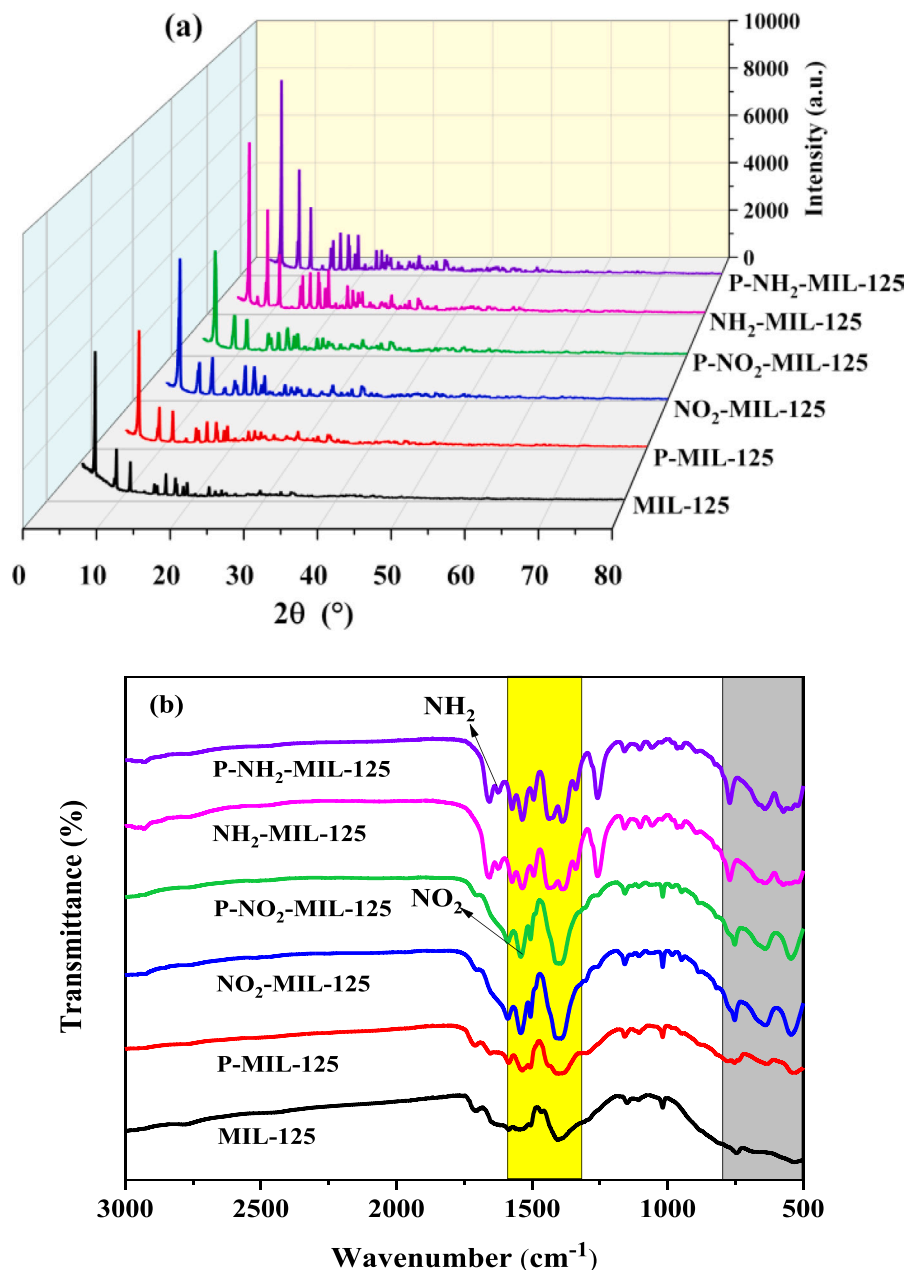


Fig. 1. (a) XRD patterns and (b) FTIR spectra of MIL-125, P-MIL-125, NO₂-MIL-125, P-NO₂-MIL-125, NH₂-MIL-125 and P-NH₂-MIL-125.

for 10 min to achieve complete dissolution of H₂BDC. Ti(OC₄H₉)₄ was added dropwise while stirring, and the mixture was stirred for 30 min and then transferred to a 50 mL Teflon liner and allowed to react at 150 °C for 24 h. The resulting suspension after the reaction was purified using DMF and MeOH, and dried at 80 °C to obtain a white solid powder. Commercial H₂BDC was replaced by P-H₂BDC, and the above synthesis procedure was followed to prepare the P-MIL-125.

P-MIL-125 with functionalized ligands was synthesized using the following procedure. NO₂-BDC (337.8 mg, 1.6 mmol) was dissolved in the mixture of DMF (18 mL) and MeOH (2 mL). Then P-MIL-125 (105.2 mg) was dispersed into the above solution by stirring, and the mixture was subsequently transferred to a 50 mL Teflon liner and reacted at 150 °C for 24 h. After cooling to room temperature, the resulting solid was collected by centrifugation, purified using DMF and MeOH, and dried at 80 °C. The obtained powder was named as P-NO₂-MIL-125. The amino modified P-MIL-125 was obtained by replacing NO₂-BDC with NH₂-BDC (289.9 mg, 1.6 mmol), which was named P-

NH₂-MIL-125. For comparison, NO₂-MIL-125 and NH₂-MIL-125 were also prepared in the same manner.

2.2. Photocatalytic performance

The photocatalytic performance of the catalysts under visible-light irradiation was evaluated in the degradation of toluene and chlorobenzene. Multiple parallel experiments were conducted to validate the experimental data. The photocatalyst (10 mg) was placed in the support of a home-built reactor, and 1 mL of liquid toluene (or chlorobenzene) was injected into it (Fig. S2). The reactor was left in the dark for 1 h to attain the adsorption equilibrium and the reaction conditions required for the complete gasification of toluene (or chlorobenzene). After the adsorption equilibrium was attained, the reaction mixture was irradiated for 1 h with a 300 W xenon lamp as a visible light source, using a 420 nm cut-off filter (420 nm < λ < 760 nm) (PLS-SXE300, Beijing Perfectlight Co., Ltd.). Firstly, the standard curve of toluene (or

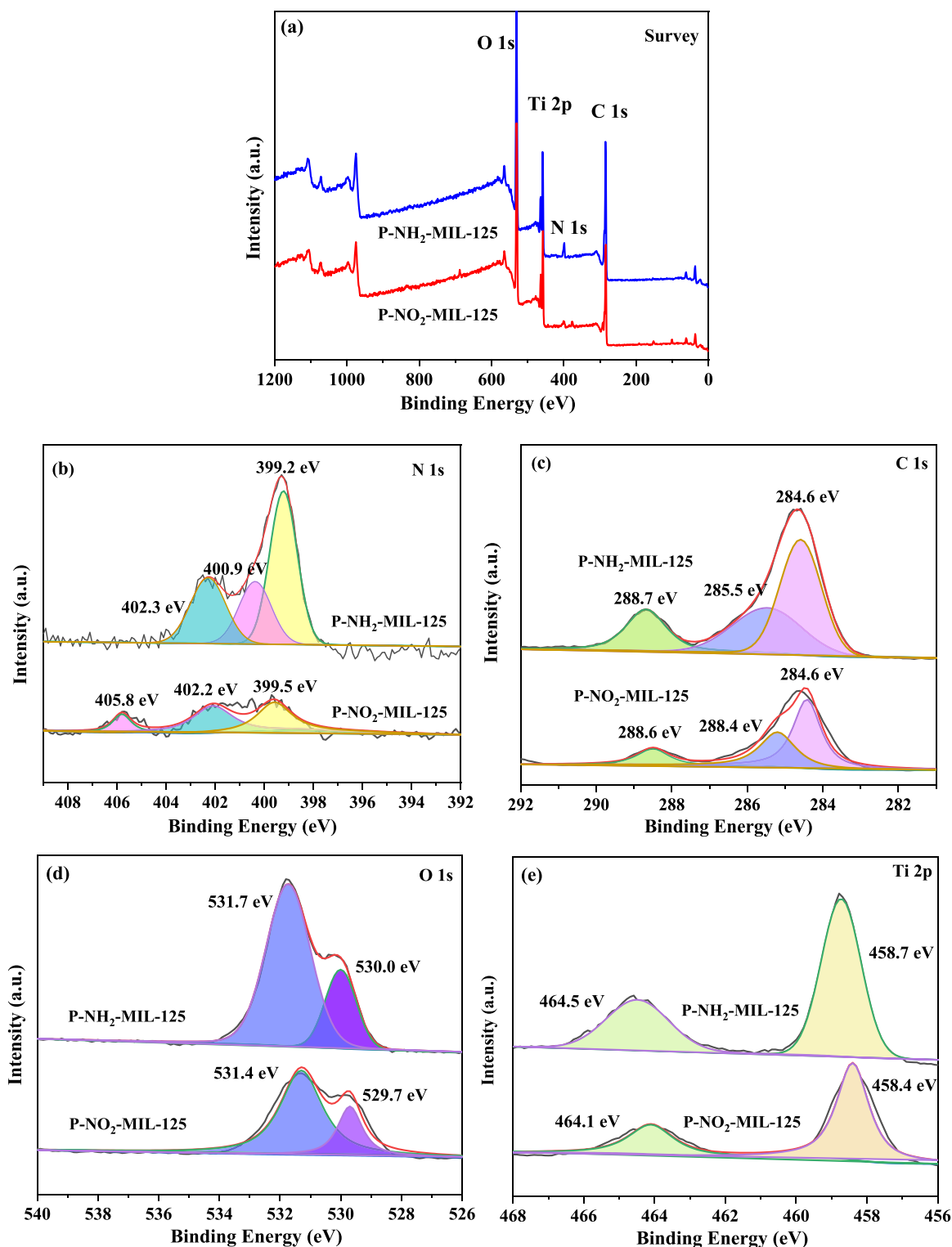


Fig. 2. XPS patterns of P-NO₂-MIL-125 and P-NH₂-MIL-125: (a) survey pattern, (b) N 1s spectra, (c) C 1s spectra, (d) O 1s spectra and (e) Ti 2p spectra.

chlorobenzene) was prepared based on the chromatographic data, 1 mL of gas was extracted from the home-built reactor using a 1 mL syringe and injected into a gas chromatograph (GC 2060, Shanghai Ruimin Instruments Co. Ltd.) to detect its concentration. The toluene (or chlorobenzene) removal rate (R) of was calculated using the following formula:

$$R = \left[1 - \left(\frac{C}{C_0} \right) \right] \times 100\% \quad (1)$$

The best activity of the samples was evaluated by fitting the curve to a pseudo-first-order kinetic equation. The pseudo first-order kinetic equation is as follow:

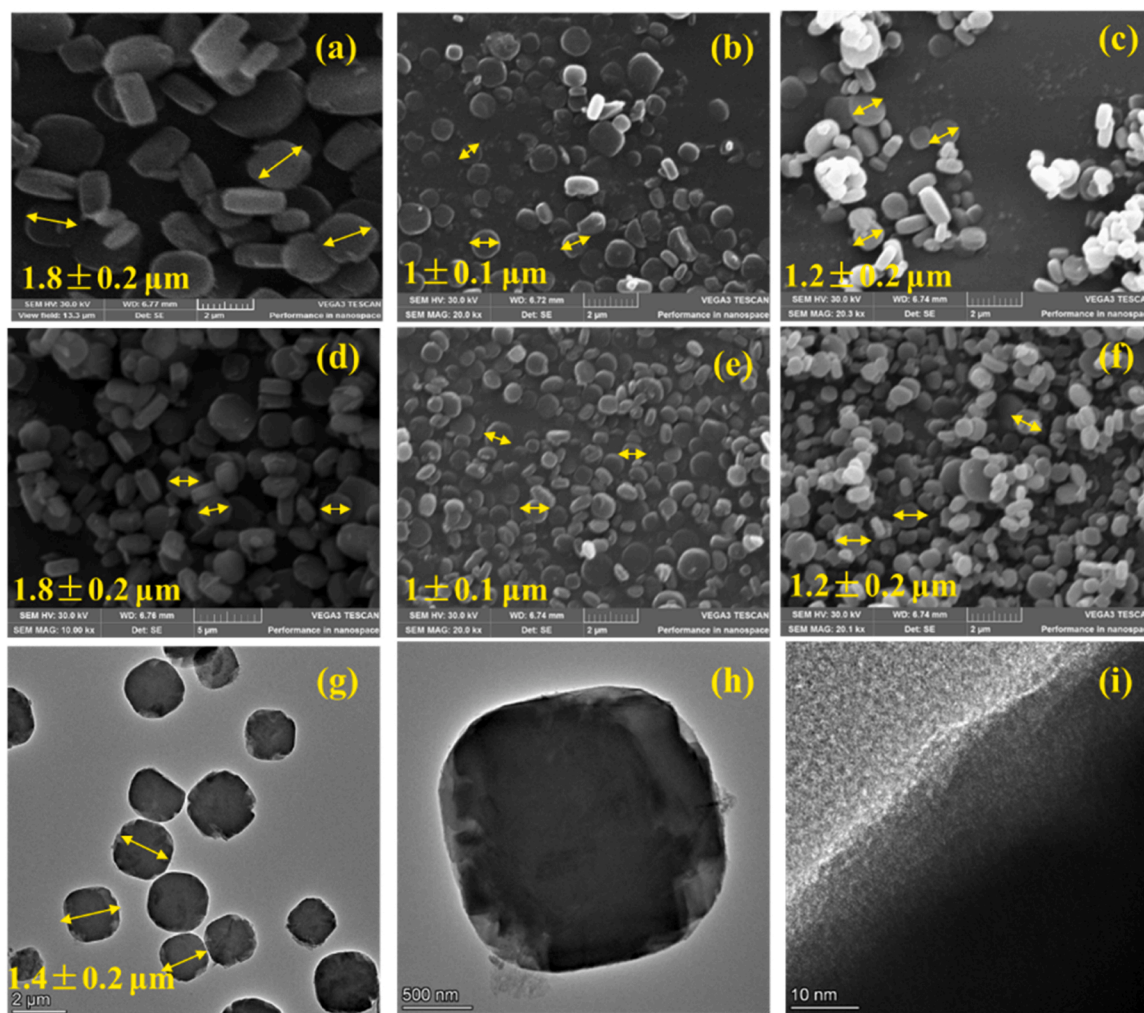


Fig. 3. SEM images of (a) MIL-125, (b) P-MIL-125, (c) NO₂-MIL-125, (d) P-NO₂-MIL-125, (e) NH₂-MIL-125, (f) P-NH₂-MIL-125 and (g,h,i) TEM images of P-NH₂-MIL-125.

$$\ln\left(\frac{C_0}{C}\right) = kt \quad (2)$$

where C and C₀ represent the initial toluene (or chlorobenzene) concentration and toluene (or chlorobenzene) concentration at time t, respectively; k is the constant (min⁻¹) of the pseudo-first-order reaction; and t is the irradiation time.

Because P-NH₂-MIL-125 exhibited the best photocatalytic performance and had a wider visible light absorption range, we further explored the possible degradation pathways of toluene and chlorobenzene using various characterization techniques including in situ FTIR spectroscopy, TG-MS and GC-MS. Specific details are reported in the [Supporting Information](#).

2.3. Scavenging experiments

In the scavenging experiments, active scavengers such as 2,2,6,6-tetramethylpiperidine oxide (TEMPO; ·OH scavenger) and benzoquinone (PBQ; ·O₂⁻ scavenger) were added to the ordinary photocatalytic degradation experiments [19]. Briefly, 10 mg of photocatalyst was mixed with 10 mg of TEMPO or PBQ, and the mixture was placed on a sample holder table for the scavenging experiments.

2.4. DFT calculations

The molecular structure of MIL-125 was geometrically optimized based on the models available in the literature [20], whereas the other molecular structures used in this work were modified by the unit cell of MIL-125, which was consistent with the actual experimental conditions. The Cambridge Sequential Total Energy Package (CASTEP) software was used for the first principles DFT calculation in Materials Studio. Additionally, all structures were optimized by Generalized Gradient Approximations (GGA) with the Perdew-Burke-Ernzerhof (PBE) function. An energy cutoff of 300 eV and a self-consistent field (SCF) tolerance of 2×10^{-6} eV/atom were used for geometry optimization, energy band structure and density of states calculations. The Brillouin zone was sampled with a $1 \times 1 \times 1$ k-point for structural optimization and calculations.

3. Result and discussion

3.1. Structure, composition, and morphology

XRD was used to characterize the crystal structures of all the samples. As shown in Fig. 1a, the diffraction peaks of MIL125 were consistent with the previously reported data [21]. The XRD pattern of P-MIL-125 was similar to that of MIL-125, indicating that functionalized MIL-125 could be successfully prepared using plastic-derived organic

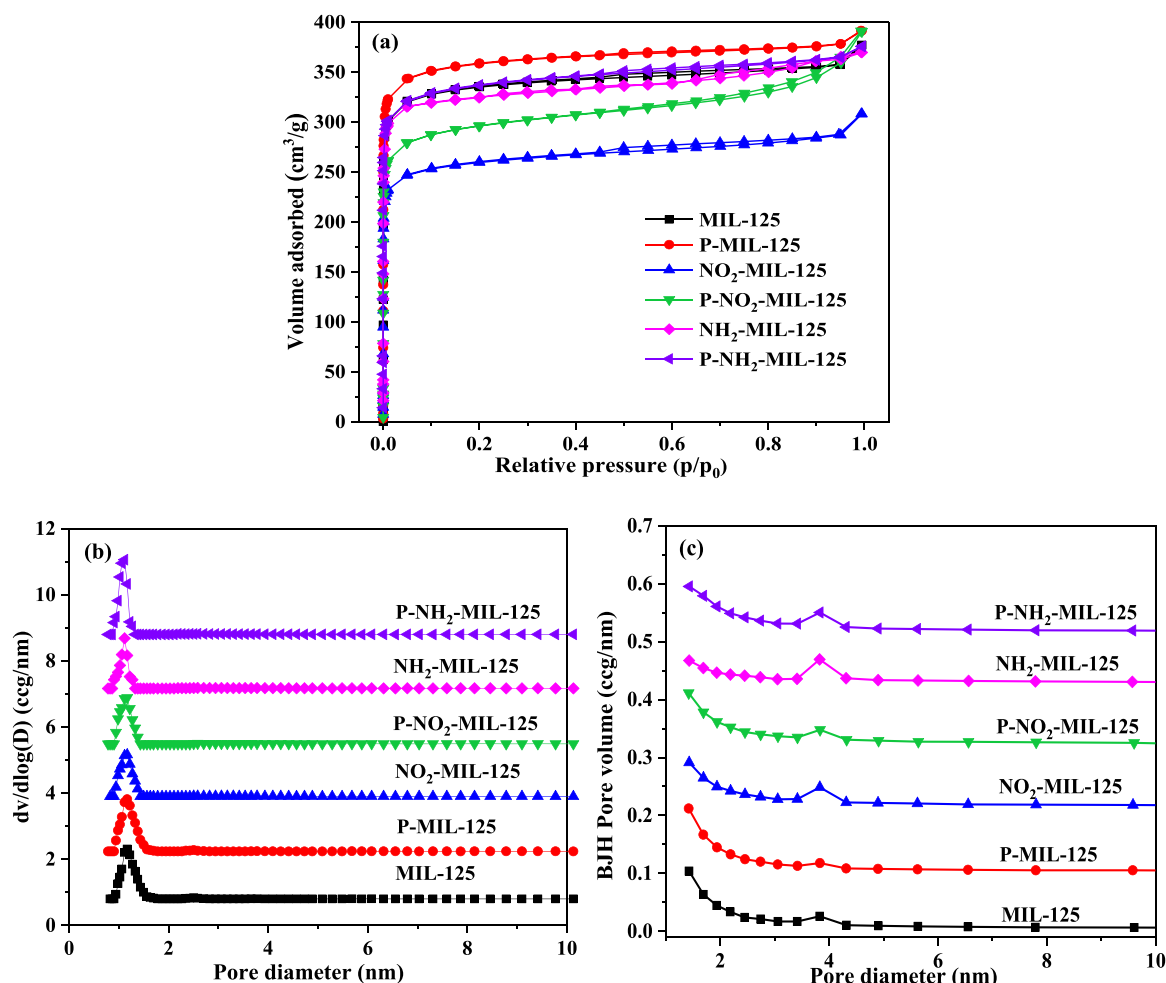


Fig. 4. (a) N₂ adsorption-desorption isotherms, (b) DFT and (c) BJH pore size distribution plots of MIL-125, P-MIL-125, NO₂-MIL-125, P-NO₂-MIL-125, NH₂-MIL-125 and P-NH₂-MIL-125.

ligands, thereby facilitating the resource utilization of plastic bottles [22]. The crystallinity was obtained by calculating the XRD spectrum (Fig. S1b), and the calculation was based on a method provided in the MDI Jade Usage Manual. The crystallinity was calculated as follows:

$$\text{Crystallinity} = \frac{\text{Area of crystalline peaks}}{\text{Area of peaks (crystalline + Amorphous)}}$$

The introduction of -NO₂ and -NH₂ did not change the crystal structure of MIL-125, and the crystallinity gradually increased. However, the crystallinity of P-NH₂-MIL-125 was slightly lower because P-H₂BDC probably contained some impurities. Huang et al. confirmed by PXRD and ¹H NMR analysis that the crystallinity of NH₂-MIL-125 was 60% [17]. Therefore, the P-NH₂-MIL-15 synthesized from P-H₂BDC had good crystallinity and could be used in a variety of applications.

FT-IR spectroscopy was performed to study the constituent chemical bonds and functional groups in the samples (Fig. 1b). The FT-IR spectra of MIL-125 and P-MIL-125 were consistent with the previously reported results [17]. The characteristic bands at 500–800 cm⁻¹ represented the O-Ti-O vibrations, while the band at 1380–1600 cm⁻¹ corresponded to carboxylates. For NH₂-MIL-125 and P-NH₂-MIL-125, there was almost no significant change in the FT-IR spectra of MIL-125 [23], except for the generation of a few additional characteristic peaks. The bands at 1642, 1334 and 1251 cm⁻¹ was attributed to the -NH₂ groups. Moreover, the N-H band was observed at 1642 cm⁻¹ [17], and the bands at 1334 and 1251 cm⁻¹ corresponded to C-N stretching vibrations [24,25]. Tang et al. found that the peak at 1540 cm⁻¹ was attributed to the asymmetric stretching vibration of nitro by the FTIR spectra of UiO-66-NO₂ [26].

Therefore, the NO₂ stretching vibration bands of NO₂-MIL-125 and P-NO₂-MIL-125 could be at 1540 cm⁻¹ [26]. It could be assumed that the -NO₂ and -NH₂ groups were successfully introduced into the MIL-125 skeleton.

The elemental composition and chemical states of P-NO₂-MIL-125 and P-NH₂-MIL-125 were investigated by XPS [27]. The full-range spectra (Fig. 2a) indicated the presence of C, N, O and Ti. The presence of the element N indicated that NO₂-BDC and NH₂-BDC were successfully replaced part of the P-H₂BDC. In P-NH₂-MIL-125, the N 1s peaks with binding energies of approximately 399.2, 400.5 and 402.3 eV could be corresponded to C-N/N-H, N-C=O and -N⁺, respectively (Fig. 2b) [28]. However, the peak of the N1s of P-NO₂-MIL-125 was in a slightly different position to that of P-NH₂-MIL-125. The peak at 399.5, 402.2 and 405.8 eV were attributed to C-N, -N⁺ and -NO₂ groups within P-NO₂-MIL-125, respectively [29]. This N1s information was demonstrated the successful introduction of the -NH₂ and -NO₂ groups into MIL-125. Furthermore, the peaks for the other elements of P-NO₂-MIL-125 remained essentially unchanged, except that the peak area was lower than that of P-NH₂-MIL-125, indicating that the -NH₂ substitution was easier than the -NO₂ substitution, which coincided with the crystallinity trend of the samples. For P-NH₂-MIL-125, the three peaks of C1s (Fig. 2c) were located at 287.7, 285.5 and 284.6 eV, corresponding to the C=O bond, C-N bond and C=C bond, respectively [30]. Moreover, the O 1s XPS peaks were shown in Fig. 2d. The two peaks at 531.7 and 530.0 eV could be attributed to -OH and Ti-O respectively [31]. The Ti 2p XPS spectrum (Fig. 2e) showed peaks for Ti 2p_{1/2} and Ti 2p_{3/2} at 464.7 eV and 458.8 eV, respectively [32].

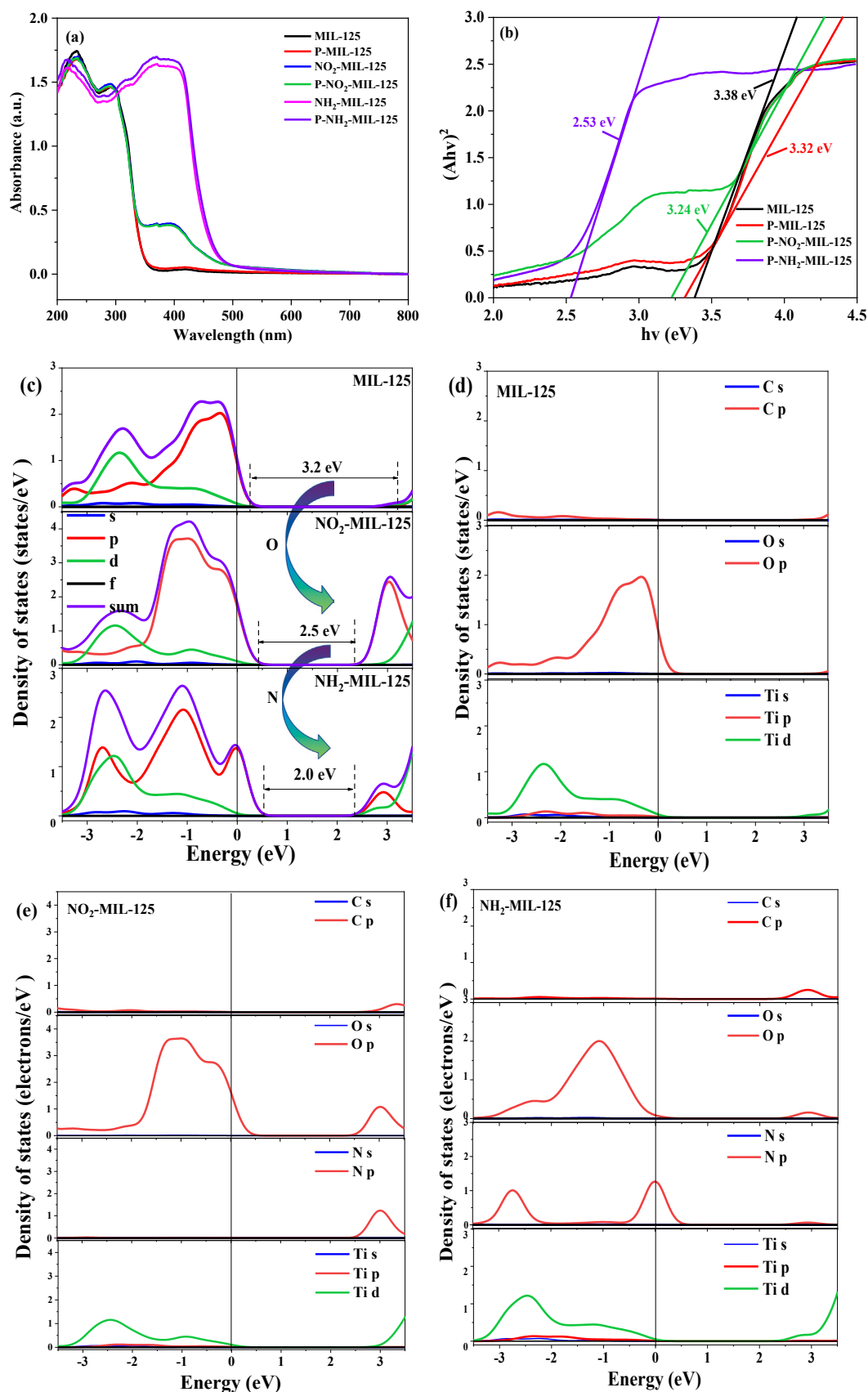


Fig. 5. (a) UV-vis of MIL-125, P-MIL-125, NO₂-MIL-125, P-NO₂-MIL-125, NH₂-MIL-125 and P-NH₂-MIL-125. (b) The relationship between $(\alpha h\nu)^{1/2}$ and its energy ($h\nu$) of MIL-125, P-MIL-125, P-NO₂-MIL-125 and P-NH₂-MIL-125. DFT calculations: (c) Total DOS and partial DOS of (d) MIL-125, (e) NO₂-MIL-125 and (f) NH₂-MIL-125.

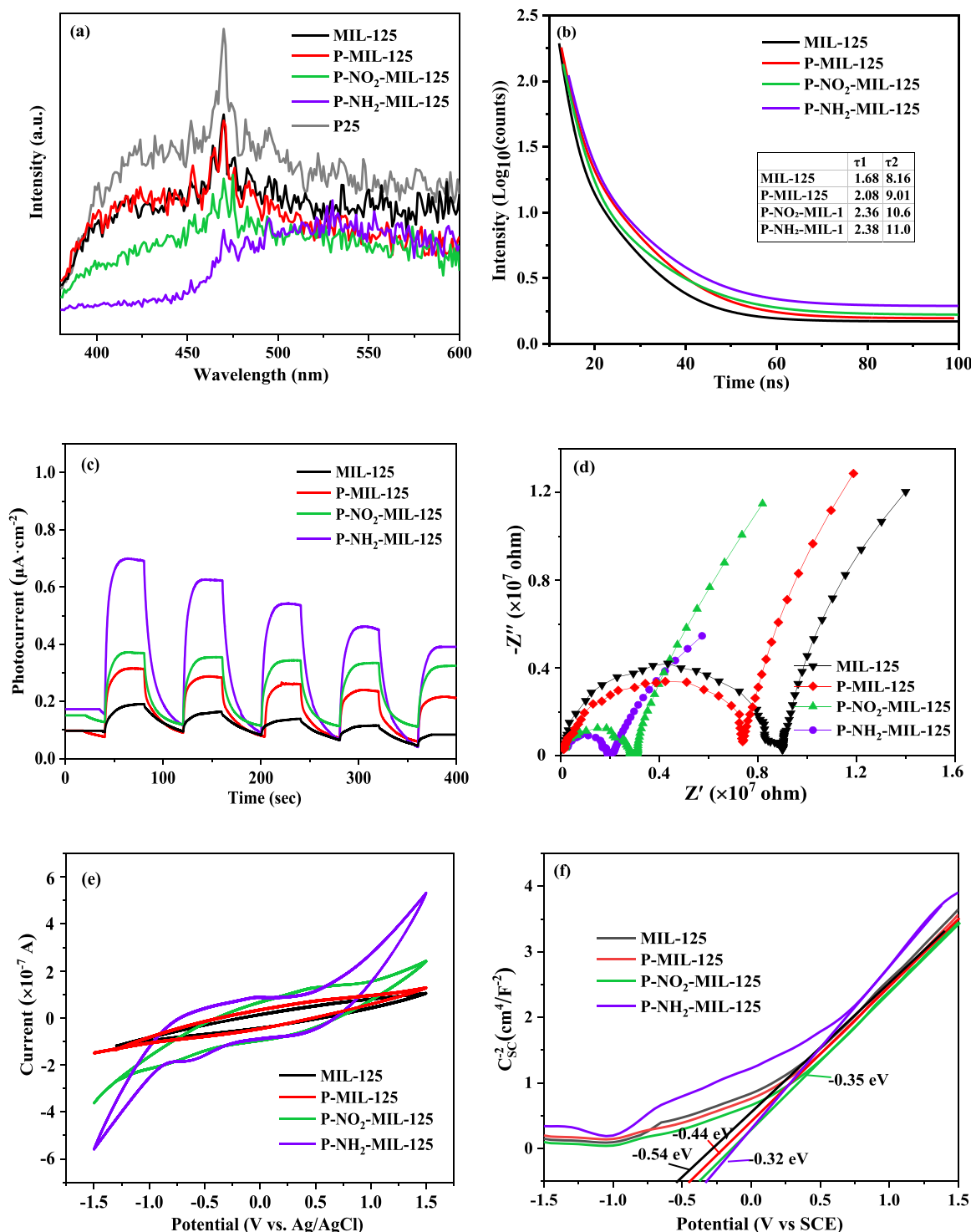


Fig. 6. (a) PL spectra, (b) time-resolved emission spectra (c) photocurrent responses, (d) the electrochemical impedance spectroscopy (EIS), (e) CV curves and (f) Mott-Schottky plots of MIL-125, P-MIL-125, P-NO₂-MIL-125 and P-NH₂-MIL-125.

Effective charge transfer between metals ($\text{Ti}^{4+} \rightarrow \text{Ti}^{3+}$) prevented further oxidation of Ti^{3+} to Ti^{4+} by the surface-adsorbed O₂ molecules ($\text{Ti}^{3+} + \text{O}_2 \rightarrow \text{Ti}^{4+} + \cdot\text{O}_2^-$). In addition, a large number of free radicals were generated. The generation of Ti^{3+} species affects the electron density distribution and induces the formation of new electronic states, thus pushing the Fermi energy level upward and enhancing the oxidation capacity [33].

The SEM images showed that both MIL-125 and P-MIL-125 had tablet-like structures with smooth surfaces (Fig. 3a, b). The average

particle size of P-MIL-125 did not differ from that of MIL-125. The average particle size was $1.8 \pm 0.2 \mu\text{m}$, suggesting that the organic ligands prepared from plastic did not destroy the morphology or alter the particle size of MIL-125. When -NH₂ and -NO₂ were introduced, the morphologies of NH₂-MIL-125, P-NH₂-MIL-125, NO₂-MIL-125 and P-NO₂-MIL-125 remained unchanged; however, the average size was slightly smaller than that of MIL-125 (Fig. 3c-f). The average particle size of NH₂-MIL-125 prepared by microwave heating was smaller due to the shorter reaction time and rapid heating, which could achieve the

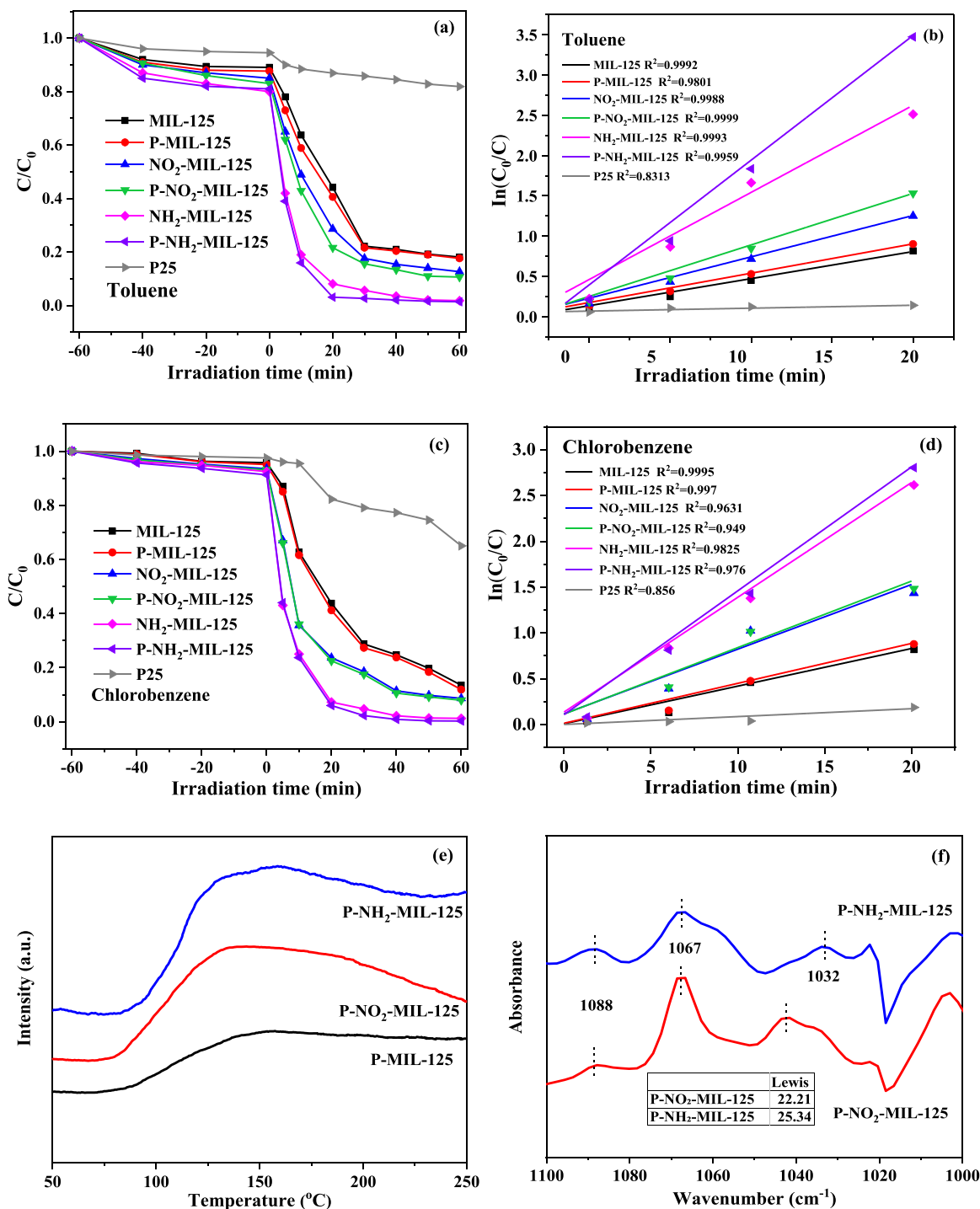


Fig. 7. (a) Curves and (b) pseudo-first-order kinetic curves of photocatalytic toluene; (c) curves and (d) pseudo-first-order kinetic curves of photocatalytic chlorobenzene; (e) the NH_3 -TPD profiles of P-MIL-125, P- NO_2 -MIL-125 and P- NH_2 -MIL-125; (f) Pyridine-IR of the obtained P- NO_2 -MIL-125 and P- NH_2 -MIL-125.

limited particle growth and promoted nucleation, respectively [34]. The small average particle size of P- NH_2 -MIL-125 and P- NO_2 -MIL-125 prepared by post-treatment might because that the $-\text{NH}_2$ and $-\text{NO}_2$ groups promoted nucleation of MIL-125 and controlled the rapid particle growth. TEM images further illustrated that P- NH_2 -MIL-125 had a tablet-like shape with a slightly smaller particle size (Fig. 3g-i).

To further study the effect of functional group modification on the porous structure of MIL-125, the N_2 absorption-desorption isotherms were recorded at 77 K (Fig. 4). The physical structure characteristics statistics were listed in Table S1. Both MIL-125 and P-MIL-125 exhibited a typical type I isotherm with an H3 hysteresis loop (Fig. 4a), indicating

that these materials are microporous [35]. The specific surface area of P-MIL-125 was $1423 \text{ m}^2 \text{ g}^{-1}$, which was slightly higher than that of MIL-125 ($1330 \text{ m}^2 \text{ g}^{-1}$). The specific surface areas of the materials decreased in the order P- NH_2 -MIL-125 > NH_2 -MIL-125 > P- NO_2 -MIL-125 > NO_2 -MIL-125. This trend could be attributed to the partial substitution of the organic ligands by NH_2 -BDC and NO_2 -BDC, which increased the skeleton size of MIL-125, thereby increasing the specific surface area [34]. Moreover, the pore size distribution of the micropores and mesopores revealed a slight reduction in the pore size of P-MIL-125 (Fig. 4b, c).

The optical absorption properties of the synthesized samples were

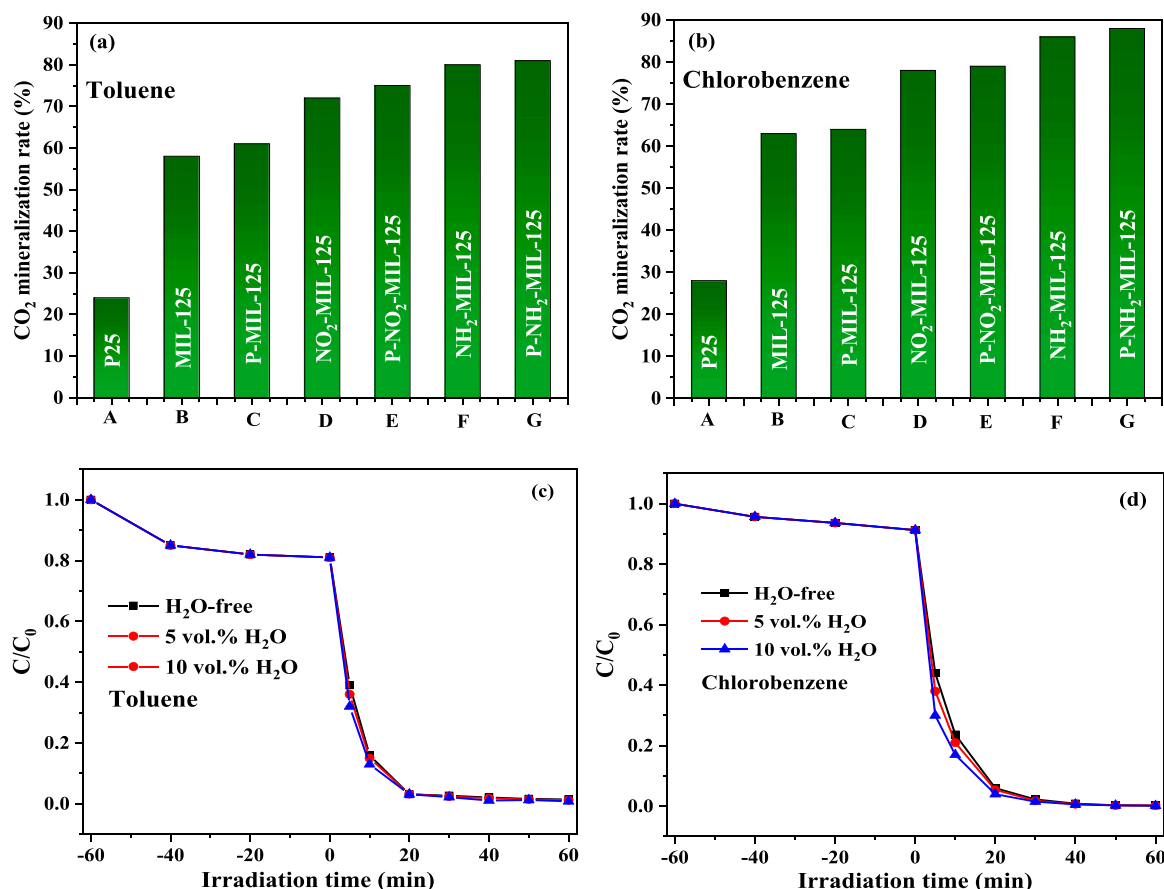


Fig. 8. The materials of the CO₂ mineralization efficiency of (a) toluene and (b) chlorobenzene; the catalytic performance of (c) toluene and (d) chlorobenzene photocatalysis over P-NH₂-MIL-125 with water vapor.

investigated by UV–vis diffuse reflectance spectroscopy (DRS). As shown in Fig. 5a, the light absorption range of MIL-125 and P-MIL-125 reached only 350 nm, suggesting response to UV light merely. Wang et al. reported that the absorption band of NH₂-MIL-125 synthesized by a modified solvothermal method, reached only 520 nm [35]. When -NH₂ and -NO₂ were introduced by post-synthetic treatment, the edges of the UV–vis absorption spectra of P-NH₂-MIL-125 and P-NO₂-MIL-125 were extended to 710 and 600 nm, respectively, demonstrating that the replacement of the ligand could effectively improve the visible light absorption range. As shown in Fig. 5b, the bandgaps of MIL-125, P-MIL-125, P-NO₂-MIL-125 and P-NH₂-MIL-125 were calculated to be 3.38, 3.32, 3.24 and 2.53 eV, respectively. Thus, the -NH₂ and -NO₂ groups could effectively improve the visible light response of MIL-125 by facilitating light absorption over a broader range of energy (i.e., wavelength), rendering it efficient for photocatalysis [36].

To gain further insights into the decrease in the band gap reduction upon the introduction of amino and nitro groups, the energy band structure and density of states (DOS) of the samples were simulated using the DFT calculations. As shown in Figs. 5c and S3, the calculated bandgaps of MIL-125, NO₂-MIL-125 and NH₂-MIL-125 were 3.2, 2.5 and 2.0 eV, respectively, which was consistent with the experimentally obtained trend. The DOS reflected the distribution of electrons in individual orbitals and the interatomic interactions, and provided insights into the chemical bonding. As shown in Fig. 5c, the VB edges of both the total orbital and partial orbital contributions of NO₂-MIL-125 and NH₂-MIL-125 were significantly lower than that of MIL-125. The s, p and d orbitals had major contributions to the VB in the range of 2.3–3.5 eV [37]. This led to a gradual reduction in the band gap after the introduction of -NO₂ and -NH₂, thereby improving the visible-light absorption by MIL-125. Furthermore, in contrast to MIL-125, the PDOS showed

that the conduction band (CB) energy level of NO₂-MIL-125 was dominated by the O orbitals, while the VB energy level of NH₂-MIL-125 was dominated by the N orbital (Fig. 5d–g). For NH₂-MIL-125, the peak of the N orbital appeared closer to the Fermi energy level, which might be easier to absorb hydrogen and more efficient in electron transfer. For NO₂-MIL-125, it was not easily added up by OH and electron transfer was hindered [38]. The above results suggested that the introduction of -NH₂ facilitated the electron transfer to the CB and stronger catalytic activity [39]. Combined experimental and theoretical calculations demonstrated that the N orbitals narrowed the VB energy level and enabled the rapid transfer of electrons to the CB. Notably, the photocatalytic activity of amino-modified MOFs generally improved in comparison to that of the unmodified MOFs [40,41]. However, the better photocatalytic performance of the amino-modified MOFs was related to the results obtained from DFT calculations and optical studies, whereas other characterizations were needed to verify the role of the N orbitals.

PL spectra were analyzed to understand the recombination rate of the charge-carriers in the samples. As shown in Fig. 6a, P-NH₂-MIL-125 exhibited the lowest PL intensity, indicating that it had the lowest recombination rate of the charge carriers [42]. TRES was used for measuring fluorescence lifetimes [17]. In Fig. 6b, all the samples had the similar decay profiles, which could be found two characteristic lifetimes τ_1 and τ_2 . In contrast, both τ_1 and τ_2 values for MIL-125 were small, representing a faster and shorter recombination process, which was consistent with the results of PL [43]. Capano et al. suggested that the slower recombination of NH₂-MIL-125 was because of the spatial separation of electrons in Ti (3d) and holes in N within the ligand [44]. However, the lifetime in P-NO₂-MIL-125 was smaller than that in P-NH₂-MIL-125, supporting the easier transfer of electrons to -NH₂ in comparison to -NO₂. To better understand the transfer and separation of

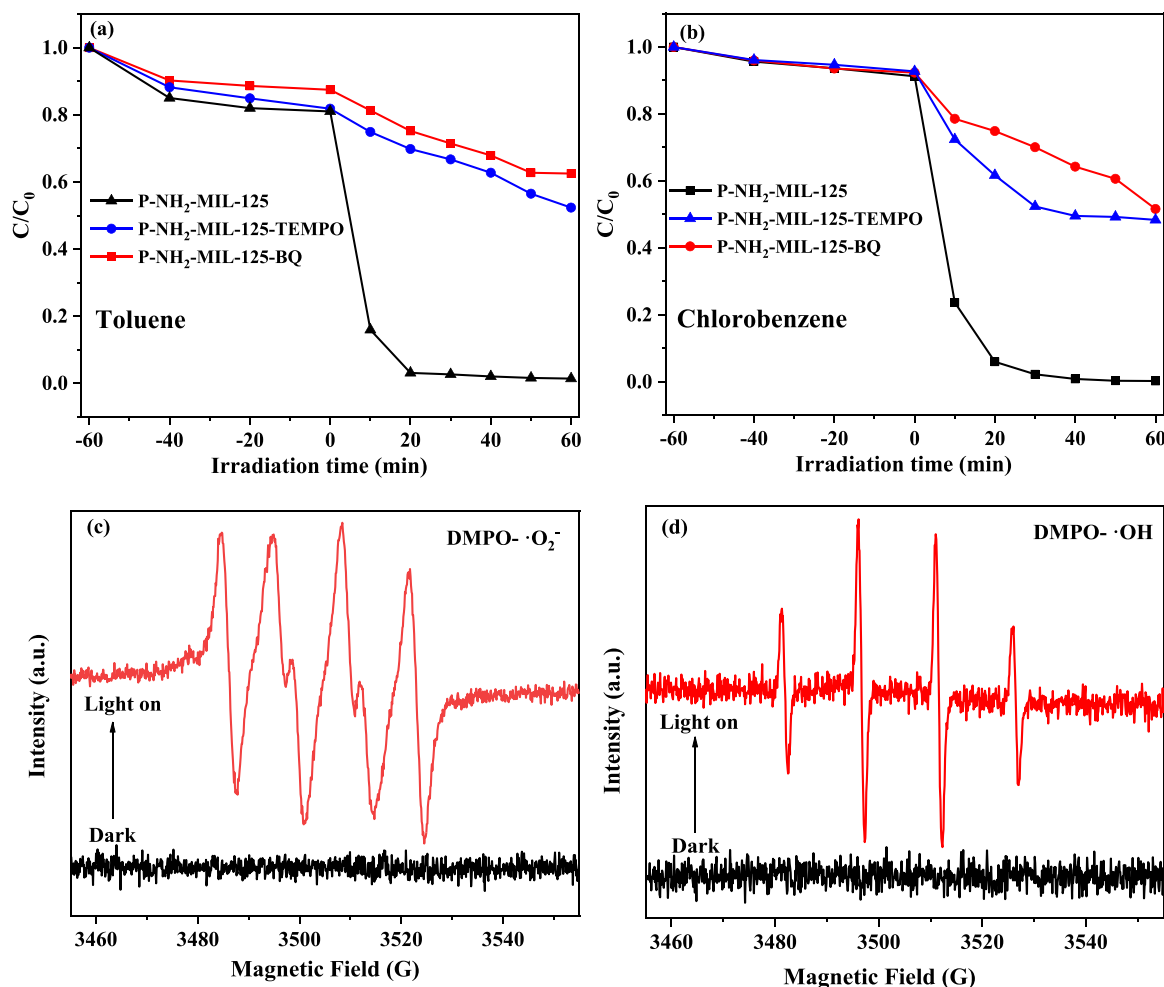


Fig. 9. Gas phase quenching experiment for degrading (a) toluene and (b) chlorobenzene by P-NH₂-MIL-125. ESR spectrum of (c) DMPO- $\cdot\text{OH}$ in aqueous media, (d) DMPO- $\cdot\text{O}_2^-$ in methanol media.

the prepared samples, transient photocurrent measurements were performed. The photoelectric properties [45] of the samples were evaluated by recording their photocurrent responses (Fig. 6c). P-NH₂-MIL-125 exhibited the highest photocurrent response signal among all the samples, indicating that it could effectively separate and transfer photo-generated electrons under visible-light irradiation. Electrochemical impedance spectroscopy (EIS) was also performed to investigate the charge carrier migration. Generally, the arc radius reflected the electron transfer resistance. The trends in Fig. 6d were consistent with the results of the transient photocurrent response [46]. Fig. 6e showed the cyclic voltammetry (CV) response of MIL-125 samples. The current values decreased in the order P-NH₂-MIL-125 > P-NO₂-MIL-125 > P-MIL-125 > MIL-125, indicating that the trend of the strength of the electron transport capability was consistent with the EIS results [45]. Furthermore, the Mott-Schottky plots of P-NH₂-MIL-125 exhibited typical n-type characteristics (Fig. 6f) [47,48]. The CB energies of MIL-125 and P-NH₂-MIL-125 were measured to be -0.32 and -0.54 eV, respectively, while the VB energies were calculated to be 3.06 and 1.99 eV, respectively, from the CB values and the band gap obtained by UV-vis DRS. The VB and CB values obtained from UV-vis DRS and Mott-Schottky plots matched with the DOS calculations. Liu et al. found that the hybridisation of Ir orbitals with Mo and S orbitals reduced the VB energy of the composite and made it easier to excite electrons from the valence band to the conduction band through PDOS [37]. From the PDOS, MIL-125 did not find the O and Ti orbitals at the VB edge, and the N orbital VB edge of NH₂-MIL-125 was clearly close to the Fermi energy level. This might be because the N orbitals hybridize with the O and Ti

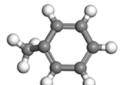

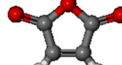
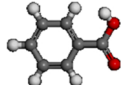
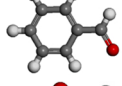
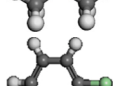
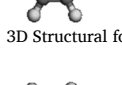
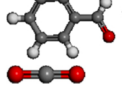
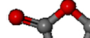
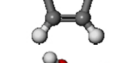
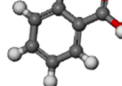
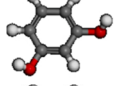
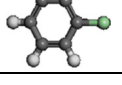
orbitals to form new energy levels, shortening the VB energy. Therefore, the significant reduction in the VB edge of NH₂-MIL-125 was due to the hybridization energy level of the N orbitals being close to the Fermi energy level.

3.2. Photocatalytic degradation of toluene and chlorobenzene

The photocatalytic activities of the MIL-125 samples under visible light were evaluated through the degradation of toluene and chlorobenzene (2000 ppm) (Fig. 7). To demonstrate the photocatalytic activities of the MIL-125 samples, P25 was used for comparison. As shown in Fig. 7a, P-NH₂-MIL-125 exhibited the highest photocatalytic activity. After 20 min of irradiation, the degradation of toluene in the presence of P-NH₂-MIL-125 reached 96%. Wang et al. synthesized the new hetero-junction photocatalyst TaON/V₂O₅ could degrade 2880 ppm toluene within 30 h [49]. Compared with other photocatalysts reported for the photocatalytic degradation of gaseous phase toluene [46, 49–51], P-NH₂-MIL-125 exhibited superior photocatalytic performance at the same concentration level in a shorter period (Table S2). The degradation of toluene over MIL-125, P-MIL-125, NO₂-MIL-125, P-NO₂-MIL-125 and NH₂-MIL-125 was 55.8%, 59.4%, 71.4%, 78.4% and 91.9%, respectively. The rate of reaction was the highest in the presence of P-NH₂-MIL-125 (Fig. 7b), indicating its strongest degradation activity. The extent of degradation and the reaction kinetics of chlorobenzene and toluene were consistent (Fig. 7c, d). Within 60 min of light exposure, P-NH₂-MIL-125 could completely degrade chlorobenzene, whereas P25 could only degrade 35% of chlorobenzene. However, the number of

Table 1

The main intermediate products identified by in-situ FTIR analysis.

Reaction substrate	Wavenumber (cm ⁻¹)	Assignment	Compound name	3D Structural formula
Toluene	3098, 3042, 2934, 2883	C-H stretching vibrations of aromatic rings and asymmetric/symmetric C-H stretching vibrations of methyl groups	Toluene	
	2367, 2327 2017, 1944, 1870	asymmetric O=C=O stretching vibration C=O stretching vibration	CO ₂ Maleic anhydride T5	 
	1605	COO- stretching vibration	Benzoic acid T4	
	1502	C-OH stretching vibration	Alcohol T2	
	1056, 1033	C-O stretching vibration	Ether species T6	
Chlorobenzene	3098, 3088, 3030, 3017	C-H stretching vibrations of aromatic rings	Chlorobenzene	
Reaction substrate	Wavenumber (cm ⁻¹)	Assignment	Compound name	3D Structural formula
Chlorobenzene	2916, 2848	C=O stretching vibrations	Benzaldehyde T3	
	2367, 2327 2088–1865	asymmetric O=C=O stretching vibration C=O stretching vibration	CO ₂ Maleic anhydride T5	 
	1746, 1645, 1592, 1485	COO- stretching vibration	Acid T4	
	1343, 1318	the in-plane bending vibration of C-OH	Phenols T11	
	1129, 1092	C-Cl asymmetric and symmetric stretching vibrations	Chlorobenzene	

Lewis and Brønsted acid sites in the catalyst during dechlorination and the reducibility for hydrocarbon oxidation were the main factors affecting the catalytic activity of photocatalytic degradation of chlorobenzene [52]. Temperature-programmed desorption of ammonia (NH₃-TPD) and the pyridine adsorbed infrared (Pyridine IR) spectrum were used to investigate the surface acidity [53,54]. Fig. 7e shows that weakly acidic NH₃ was adsorbed on the catalyst surface. Moreover, the peak intensity of P-NH₂-MIL-125 was the highest among all the samples, indicating that this material had the highest total acid content and the strongest acidic activity. Furthermore, the photocatalytic performance of NH₂-MIL-125 improved slightly upon replacing the organic ligand with P-H₂BDC, probably because P-H₂BDC was not 100% pure and remained weakly acidic. Thus, P-NH₂-MIL-125 was more acidic, and P-NH₂-MIL-125 synthesized from the mixture of P-H₂BDC and NH₂-BDC had a better photocatalytic effect on chlorobenzene degradation. The content of the Lewis acidic site plays a dominant role in catalyzing the chlorobenzene reaction [55]. Further Pyridine IR studies were carried out to distinguish between Lewis and Brønsted acid sites on P-NH₂-MIL-125 and P-NO₂-MIL-125 (Fig. 7f) [56]. Typically, the

1400–1600 cm⁻¹ band identifies Lewis and Brønsted acid sites. However, it is not visible in the case of MOF materials with stronger bands due to carboxylate and ring vibrations. Leclerc et al. focused on the 1100–1000 cm⁻¹ spectral band to evaluate the variation in Lewis intensity of MIL-100(Fe) [57]. The content of Lewis acid in P-NH₂-MIL-125 and P-NO₂-MIL-125 were 25.34 and 22.21, respectively, which was consistent with the order of their catalytic performances. Interestingly, the order of catalytic performance was consistent with the BET specific surface area. The enlargement of the catalyst pore size and volume enabled the catalytic efficiency of the active sites located in the carrier channels [58]. In addition, the large BET surface area exposed more Lewis active sites to facilitate the adsorption of toluene and chlorobenzene on the surface.

Fig. 8a, b showed the mineralization efficiency of the catalysts for the degradation of toluene and chlorobenzene. The complete mineralization of toluene produces CO₂ and H₂O, and the mineralization efficiency ϕ (%) for toluene and chlorobenzene was calculated by measuring the CO₂ concentration after equilibrium [59], using the following equation:

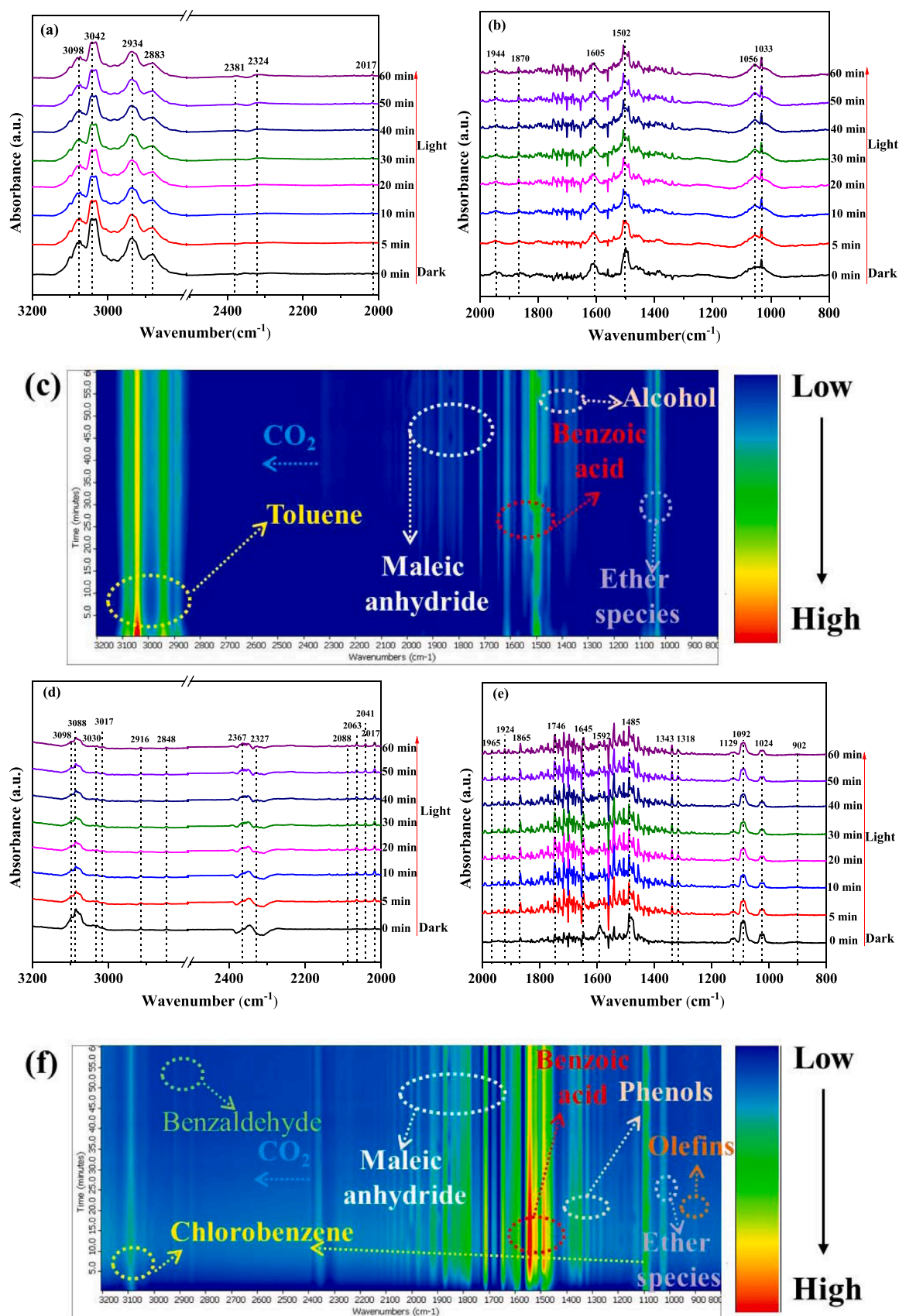


Fig. 10. In situ FTIR spectra recorded as a function of irradiation time for degradation of gaseous (c) toluene (the bands recorded in the range of (a) 3300–2000 cm^{-1} and (b) 2000–800 cm^{-1}), and (f) chlorobenzene (the bands recorded in the range of (d) 3300–2000 cm^{-1} and (e) 2000–800 cm^{-1}).

Table 2

The main intermediate products identified by the GC-MS instrument.

Reaction substrate	Time	Molecular formula	Compound name	3D Structural formula	Ion debris (<i>m/z</i>)
Toluene	3.726	C ₂ H ₆ O	Ethanol T2		45, 46, 73
	10.224	C ₇ H ₈	Toluene		91
Chlorobenzene	3.790	CH ₂ O ₂	Formic acid T10		45
	4.542	C ₂ H ₆ O	Ethanol T2		45, 46, 73
	4.736	C ₄ H ₁₀ O ₃	Diethylene glycol T14		45, 75
	5.827	C ₅ H ₁₀ O ₂	Propyl acetate T13		43, 61, 73
	5.980	C ₄ H ₈ O ₄	1,3,5,7-Tetroxocane T14		44, 61, 91
	13.553	C ₆ H ₅ Cl	Chlorobenzene		77, 112

$$\varphi = \frac{C_c}{3.34 \times (C_s - C_c)} \times 100\% \quad (3)$$

Here, C_c is the actual CO₂ concentration produced by degradation (mg m⁻³); C_s and C_c represent the initial and final toluene or chlorobenzene concentrations in the reactor, respectively, mg m⁻³; 3.34 ($C_s - C_c$) is the theoretical CO₂ production (mg m⁻³). The CO₂ concentration was gradually increased upon the light irradiation. In addition, the CO₂ yield in the presence of P-NH₂-MIL-125 for toluene and chlorobenzene was significantly higher than in the presence of MIL-125, indicating that the introduction of -NH₂ improved the mineralization efficiency of MIL-125 for toluene and chlorine to generate CO₂. Wang et al. prepared a novel heterojunction photocatalyst for the degradation of toluene to produce 2298 ppm CO₂ within 30 h [49]. P-NH₂-MIL-125 could mineralize 80% of toluene and chlorobenzene in a shorter period time indicating its superior photocatalytic performance. Fig. 8c, d showed the degradation curves of P-NH₂-MIL-125 on toluene and chlorobenzene after the introduction of water vapor. The degradation rates of toluene and chlorobenzene did not change, after adding a certain amount of water vapor, indicating that P-NH₂-MIL-125 was resistant to water to some extent.

Toluene recycling degradation experiments were performed to test the stability of P-NH₂-MIL-125. The degradation of toluene in the presence of P-NH₂-MIL-125 remained above 90% after four cycles (Fig. S4a). The excellent recyclability of P-NH₂-MIL-125 could be attributed to the rapid diffusion of toluene and the products from the active sites on the outer surface, which prevented catalyst deactivation due to the blocking of pores by the product [60]. The XRD patterns of P-NH₂-MIL-125 before and after the reaction remained almost unchanged (Fig. S4b), demonstrating that the framework structure and crystallinity of the catalysts were retained. Thus, the P-NH₂-MIL-125 catalyst exhibited good stability and water resistance.

3.3. Mechanisms of photocatalytic degradation of toluene and chlorobenzene

Scavenging experiments were performed to assess the photocatalytic performance of P-NH₂-MIL-125 in the production of active species and

to explore the mechanism of the photocatalytic degradation. To identify the main active species in the photocatalytic degradation, scavenger experiments were conducted; TEMPO was used as an ·OH trapping agent and BQ was used as an ·O₂⁻ trapping agent [19]. The extent of photocatalytic degradation significantly reduced when TEMPO and BQ were added (Fig. 9a, b), indicating that the ·O₂⁻ and ·OH radicals had the leading role in the photocatalytic degradation of toluene and chlorobenzene. To further explore the dominant reactive species, the EPR spectrum of P-NH₂-MIL-125 was obtained using DMPO as a spin trap reagent under visible-light excitation [61]. As shown in Fig. 9c, d, the intensities of DMPO-·O₂⁻ and DMPO-·OH of P-NH₂-MIL-125 was almost negligible under dark conditions, whereas the intensity increased significantly upon light irradiation. Therefore, ·O₂⁻ and ·OH radicals were the main active species in the photocatalytic degradation of toluene and chlorobenzene, thereby validating the results of the scavenging experiments.

Therefore, the main reactive oxygen radicals during the photoreaction of ·O₂⁻ and ·OH and the degradation mechanisms of toluene and chlorobenzene could be clearly inferred from the scavenging experiments and theoretical calculations. After the introduction of the amino group, the N atomic orbitals hybridized with other atomic orbitals of MIL-125, driving the impurity energy level closer to the Fermi energy level, thereby narrowing the bandgap [33,39]. Therefore, the band gap of MIL-125 decreased from 3.32 to 2.53 eV. Consequently, electrons were more easily excited from the VB to the CB, and reacted with H₂O and O₂ to generate more ·O₂⁻ and ·OH [62,63].

The intermediate species produced during the photocatalysis of toluene and chlorobenzene on P-NH₂-MIL-125 were determined by in situ FTIR spectroscopy, GC-MS and TG-MS [64,65]. In situ FTIR spectroscopy was used to examine the changes in the structure of the functional groups during the reaction (Table 1). In Fig. 10a, b, the in-situ FTIR bands in the range of 3200–800 cm⁻¹ corresponded to toluene degradation. The bands at 3098, 3042, 2934 and 2883 cm⁻¹ represented the C-H stretching vibrations of aromatic rings and the asymmetric/symmetric C-H stretching vibrations of the methyl groups. The peak intensity of toluene gradually decreased upon irradiation, indicating its degradation [66]. In addition, new characteristic peaks were generated during photodegradation. The signals at 2381 and 2324 cm⁻¹ were

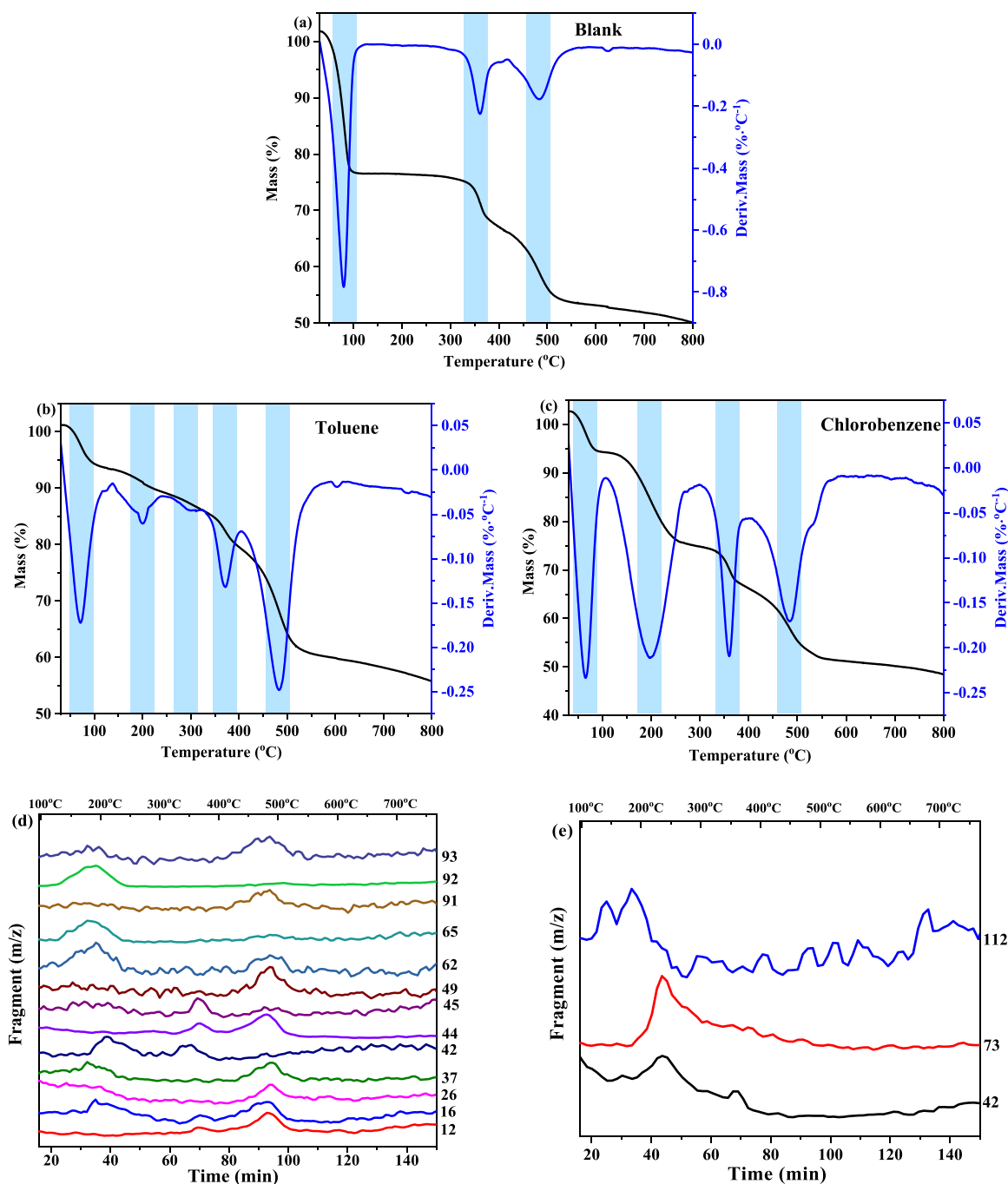


Fig. 11. TG-DTG spectra of (a) P-NH₂-MIL-125, and P-NH₂-MIL-125 after photodegradation of (b) toluene and (c) chlorobenzene; MS signals of gaseous products evolved during photocatalytic degradation of (d) toluene and (e) chlorobenzene.

ascribed to asymmetric O=C=O stretching vibrations, indicating the production of CO₂ during photocatalysis. The weak adsorption bands at 2017, 1944 and 1870 cm⁻¹ could be assigned to C=O stretching vibration, which was the characteristic of maleic anhydride (T5) [67]. The absorption peaks at 1605 and 1502 cm⁻¹ were attributed to COO- and C-OH stretching vibrations, respectively. These new absorption peaks demonstrated that the C-H bond of the methyl group on the aromatic ring was cleaved to form a C-O bond, producing intermediate products of benzoic acid (T4) and alcohol (T2) [68]. The peaks at 1056 and 1033 cm⁻¹ were associated with the C-O stretching vibration of ether species [69]. Certainly, the changes in toluene, CO₂ and the possible intermediates during the reaction could be identified by color gradation (Fig. 10c). The above results led to the hypothesis that the adsorbed

toluene molecules reacted with the oxygen reactive groups on the catalyst surface to produce intermediate products such as T2, T4, T5, T6 and CO₂. During the photocatalytic degradation of chlorobenzene species other than the intermediate products of toluene degradation were also produced. The peaks at 3098, 3088, 3030 and 3017 cm⁻¹ were attributed to the C-H stretching vibrations of the aromatic rings, and the decrease in these peak intensities indicated the degradation of chlorobenzene. The bands at 1129 and 1092 cm⁻¹ were assigned to C-Cl asymmetric and symmetric stretching vibrations, respectively. With increasing irradiation time, the weak peaks at 2916 and 2848 cm⁻¹ gradually became apparent. These peaks were attributed to C=O stretching vibrations, indicating the presence of benzaldehyde (T3) [70]. In addition, the peaks at 2367 and 2327 cm⁻¹ were attributed to

Table 3

The main intermediate products identified by the TG-MS instrument.

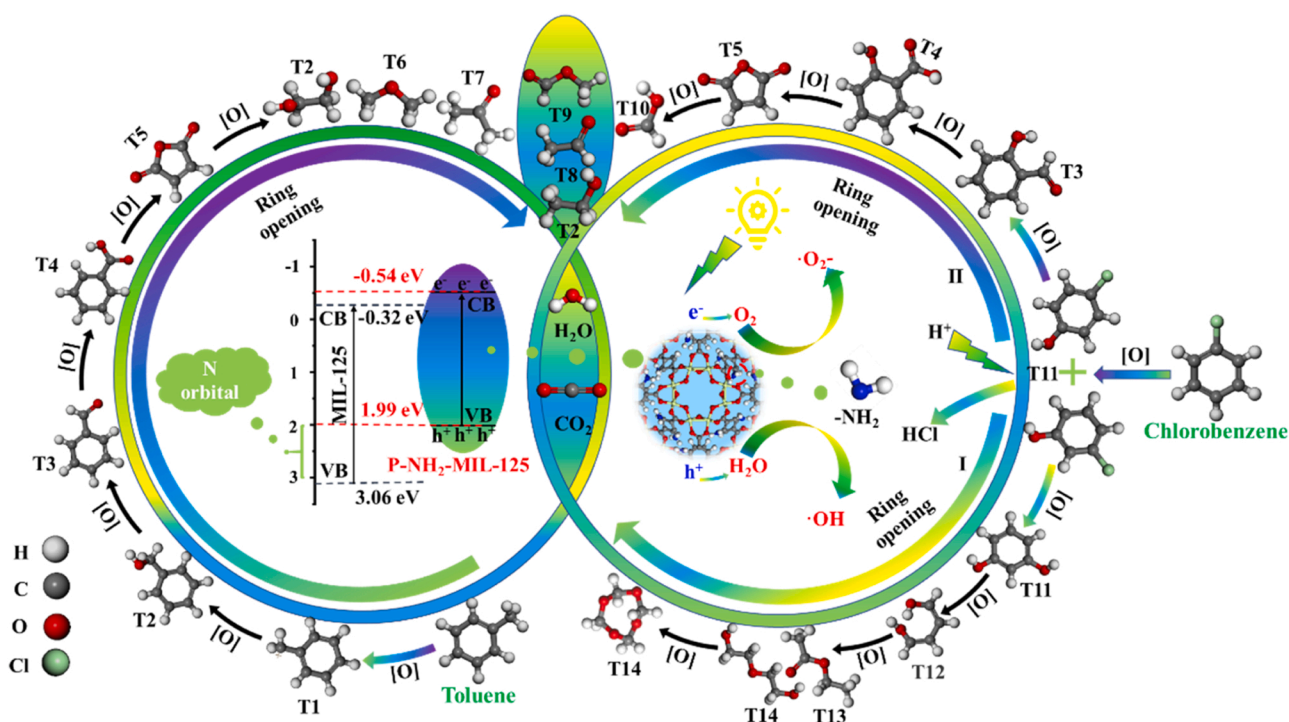
Reaction substrate	Main fragment (m/z)	Desorption temperature ($^{\circ}\text{C}$)	Possible intermediates	Detection in sample
Toluene	12, 16, 26, 37, 49	485	Simple hydrocarbons	C_xH_y
	42	214, 350	Acetaldehyde T8	$\text{C}_2\text{H}_4\text{O}$
	44	370	Carbon dioxide	CO_2
	45	366	Ethyl ether T6	$\text{C}_2\text{H}_6\text{O}$
	50, 51	178	Ketones T7	$\text{C}_3\text{H}_6\text{O}$
	58, 59	225	Methyl formate T9	$\text{C}_2\text{H}_4\text{O}_2$
	62, 63, 65	198	Alcohols T2	$\text{C}_2\text{H}_6\text{O}_2$
	92	187	Toluene	C_7H_8
	93	487	Phenylmethyl T1	C_7H_8^+
	15	240	Methyl	CH_3^+
	42	238, 361	Acetaldehyde T8	$\text{C}_2\text{H}_4\text{O}$
	58, 59	175	Methyl formate T9	$\text{C}_3\text{H}_8\text{O}$
Chlorobenzene	73	235	Propyl acetate T13	$\text{C}_4\text{H}_{10}\text{O}_2$
	112	138, 191	Chlorobenzene	$\text{C}_6\text{H}_5\text{Cl}$

the formation of CO_2 (Fig. 10d, e). The peaks in the range of $2100\text{--}1865\text{ cm}^{-1}$ were assigned to T5. The absorption peaks at 1746 , 1645 , 1592 and 1485 cm^{-1} were the characteristic peaks of T4. The peaks at 1343 and 1318 cm^{-1} were associated with the in-plane bending vibration of C-OH, indicating the generation of phenol (T11). The peak of 1024 cm^{-1} was assigned to the C-O stretching vibration of the adsorbed ether (T14). Notably, a weak peak was observed at 902 cm^{-1} , which might be attributed to the C=C stretching vibration of olefins (T12). Thus, the changes in chlorobenzene and the possible intermediates formed during its degradation could be obtained (Fig. 10f).

GC-MS, which gave an estimate of the mass-to-charge ratio of the sample ions, was a qualitative and quantitative method for analyzing intermediates. TG-MS was performed by thermogravimetric heating of

the sample to produce volatile gases. To analyze the intermediate products, the volatile gases were transferred to a mass spectrometer for identification [65,71]. The residue on the surface of P-NH₂-MIL-125 after the reaction was extracted with methanol solution, and identified by GC-MS. The GC-MS results were summarized in Table 2 and Fig. S5. Only ethanol (T2) was identified by GC-MS during the photocatalytic degradation of toluene. During the degradation of chlorobenzene, five intermediate products were identified, namely T2, formic acid (T10), propyl acetate (T13), diethylene glycol and 1,3,5,7-tetroxocane (T14). P-NH₂-MIL-125 was heated thermogravimetrically and then transferred to a mass spectrometer for analysis of the intermediate products. P-NH₂-MIL-125 decomposed on its own with increasing temperature (Fig. 11a). TG-differential thermogravimetry (DTG) analysis showed that P-NH₂-MIL-125 underwent mass loss in two stages and one stage after toluene and chlorobenzene degradation, respectively. This contrasted with the behavior of P-NH₂-MIL-125 before the reaction (Fig. 11b, c). The species adsorbed on the surface of the sample after the reaction of toluene and chlorobenzene were listed in Table 3; a comparison with those before the reaction had also been presented. The following intermediate species were desorbed from P-NH₂-MIL-125 at high temperatures after the toluene reaction (Fig. 11d and S6): $m/z = 12, 16, 26, 37, 49$ (hydrocarbons), 42 (acetaldehyde T8), 44 (CO_2), 45 (ether T6), 50, 51 (acetone T7), 58, 59 (methyl formate T9), 62, 63, 65 (alcohols T2), 92 (toluene) and 93 (benzyl T1). The following fragments were detected on the surface of P-NH₂-MIL-125 after the chlorobenzene reaction (Fig. 11e and S6): $m/z = 15$ (methyl), 42 (T8), 58, 59(T9), 73 (propyl acetate T13), and 112 (chlorobenzene).

The analysis of intermediates is important for the study of degradation pathways, however, the rapid changes in intermediates prevent them from being captured and the degradation pathways cannot be studied in depth. Although the photocatalytic degradation of toluene and chlorobenzene has been extensively studied in the literature, few studies have speculated on the degradation pathways of toluene and chlorobenzene by combining with the intermediates obtained during and after the reaction [72,73]. The degradation pathways were deduced based on the intermediates analyzed by DFT calculations, EPR, in situ FTIR spectroscopy, GC-MS and TG-MS (Scheme 2). Toluene lost

**Scheme 2.** Possible catalytic mechanisms and pathways for toluene and chlorobenzene over P-NH₂-MIL-125.

electrons to form a benzyl species (T1), which was then sequentially converted into benzyl alcohol (T2), benzaldehyde (T3), and benzoic acid (T4) under the influence of active oxygen groups. The aromatic ring of T4 opened under the action of -OH to produce the isomerized product maleic acid (T5). The -OH radicals continued to attack the isomerized products, offering small molecules such as ether (T6), ethylene glycol (T2), acetone (T7), acetaldehyde (T8) and methyl formate (T9). Finally, these small molecules were completely oxidized to hydrocarbons, CO₂ and H₂O.

For chlorobenzene, the active oxygen groups directly attacked the hydrogen atoms on the benzene ring, and the -OH radicals replaced the hydrogen atoms to generate chlorophenol compounds (T11). The substitution of Cl atoms due to nucleophilic interactions led to the formation of bisphenol species and the decomposition of rings. The ring was then opened to generate small molecules such as olefins (T12), propyl acetate (T13) and diethylene glycol (T14). The instability of these small molecules and ester-alcohol binding led to the formation of 1,3,5,7-tetraoxane (T14), which was eventually oxidized to produce CO₂ and H₂O. NH₃-TPD and pyridine IR measurements suggested that P-NH₂-MIL-125 contained more acidic sites. Cl atoms could be adsorbed at the Lewis acidic sites, and these Cl atoms could combine with the H⁺ at the acidic site and convert to HCl gas [74,75]. In contrast, chlorophenols (T11) were oxidized to salicylic acids (T3) by superoxide radicals, and the subsequent degradation pathway was similar to that of toluene. Small molecules such as T2, T5, T8, T9 and formic acid (T10) were produced in a stepwise manner to finally generate CO₂ and H₂O.

4. Conclusion

In conclusion, we successfully synthesized a series of functional group-modified MIL-125 using plastic bottles as the organic ligand for the efficient degradation of toluene and chlorobenzene. DFT calculations and optical studies showed that the hybridization energy level of the N orbitals was close to the Fermi energy level, which shortened the band gap of MIL-125, thus facilitating easier hydrogen absorption and rapid electron transfer from VB to CB. The N 1 s XPS spectrum, electrochemical and TRES analysis further found that P-NH₂-MIL-125 exhibited a lower electron density, the lower impedance, higher photocurrent response and longer fluorescent lifetime in comparison to P-NO₂-MIL-125. Moreover, the results combined with NH₃-TPD and pyridine IR, P-NH₂-MIL-125 synthesized using P-H₂BDC had more Lewis acidic sites to rapidly adsorb toluene and chlorobenzene. Moreover, P-NH₂-MIL-125 exhibited excellent recyclability and water resistance. DFT calculations, EPR spectroscopy, in situ FTIR spectroscopy, GC-MS and TG-MG analysis were performed to elucidate the possible toluene and chlorobenzene degradation pathways. Thus, this work demonstrates an economically feasible strategy for modifying MOFs and suggests the possible VOC degradation pathways.

CRedit authorship contribution statement

Xiaodong Zhang: Writing – original draft, Conceptualization, Writing – review & editing, Funding acquisition. **Ke Yue:** Writing – original draft. **Renzhi Rao:** Data curation and analysis. **Jinfeng Chen:** Software, Data curation. **Qiang Liu:** Data curation. **Yang Wang:** Data curation. **Fukun Bi:** Visualization, Investigation. **Yuxin Wang:** Validation, Funding acquisition. **Jingcheng Xu:** Software. **Ning Liu:** Writing – review & editing.

Declaration of Competing Interest

The authors declare that they have no known competing financial interests or personal relationships that could have appeared to influence the work reported in this paper.

Acknowledgements

This work is sponsored financially by the National Natural Science Foundation of China (No.21906104 and No.12175145), the Shanghai Rising-Star Program (21QA1406600) and Natural Science Foundation of Shanghai (19ZR1434900); and is provided technical support by “Ceshigo Research Services Agency for XPS, EPR, Pyridine IR and TG-MS, www.ceshigo.com”.

Appendix A. Supporting information

Supplementary data associated with this article can be found in the online version at doi:10.1016/j.apcatb.2022.121300.

References

- [1] Y. Yang, S. Zhao, L. Cui, F. Bi, Y. Zhang, N. Liu, Y. Wang, F. Liu, C. He, X. Zhang, Recent advancement and future challenges of photothermal catalysis for VOCs elimination: from catalyst design to applications, *Green Energy Environ.* (2022), 101843, <https://doi.org/10.1016/j.surfin.2022.101843>.
- [2] A. Jafari, M. Moslemzadeh, A. Esrafil, R. Kalantary, Synthesis of new composite based on TiO₂ immobilized in glass fibers for photo-catalytic degradation of chlorobenzene in aqueous solutions, *Environ. Res.* 204 (2022), 112018, <https://doi.org/10.1016/j.envres.2021.112018>.
- [3] K. Yue, X. Zhang, S. Jiang, J. Chen, Y. Yang, F. Bi, Y. Wang, Recent advances in strategies to modify MIL-125 (Ti) and its environmental applications, *J. Mol. Liq.* 335 (2021), 116108, <https://doi.org/10.1016/j.molliq.2021.116108>.
- [4] L. Qiu, H. Li, F. Dai, F. Ouyang, D. Pang, H. Wang, Adsorption and photocatalytic degradation of benzene compounds on acidic F-TiO₂/SiO₂ catalyst, *Chemosphere* 246 (2020), 125698, <https://doi.org/10.1016/j.chemosphere.2019.125698>.
- [5] W. Gao, Z. Wang, C. Peng, S. Kang, L. Cui, Accelerating the redox kinetics by catalytic activation of “dead sulfur” in lithium–sulfur batteries, *J. Mater. Chem. A* 9 (2021) 13442–13458, <https://doi.org/10.1039/D1TA00772F>.
- [6] Q. Zhao, Q. Du, Y. Yang, Z. Zhao, J. Cheng, F. Bi, X. Shi, J. Xu, X. Zhang, Effects of regulator ratio and guest molecule diffusion on VOCs adsorption by defective UiO-67: experimental and theoretical insights, *Chem. Eng. J.* 433 (2022), 134510, <https://doi.org/10.1016/j.cej.2022.134510>.
- [7] Q. Du, R. Rao, F. Bi, Y. Yang, W. Zhang, Y. Yang, N. Liu, X. Zhang, Preparation of modified zirconium-based metal-organic frameworks (Zr-MOFs) supported metals and recent application in environment: a review and perspectives, *Surf. Interfaces* 28 (2022), 101647, <https://doi.org/10.1016/j.surfin.2021.101647>.
- [8] X. Zhang, F. Bi, Z. Zhu, Y. Yang, S. Zhao, J. Chen, X. Lv, Y. Wang, J. Xu, N. Liu, The promoting effect of H₂O on rod-like MnCeOx derived from MOFs for toluene oxidation: a combined experimental and theoretical investigation, *Appl. Catal. B Environ.* 297 (2021), 120393, <https://doi.org/10.1016/j.apcatb.2021.120393>.
- [9] S. Jiang, Z. Zhao, J. Chen, Y. Yang, C. Ding, Y. Yang, Y. Wang, N. Liu, L. Wang, X. Zhang, Recent research progress and challenges of MIL-88(Fe) from synthesis to advanced oxidation process, *Surf. Interfaces* 30 (2022), 101843, <https://doi.org/10.1016/j.surfin.2022.101843>.
- [10] D. Panda, S. Patra, M. Awasthi, S. Singh, Lab Cooked MOF for CO₂ Capture: A sustainable solution to waste management, *J. Chem. Educ.* 97 (2020) 1101–1108, <https://doi.org/10.1021/acs.jchemed.9b00337>.
- [11] A. Aguado, L. Martínez, L. Becerra, M. Arieta-araunabeña, S. Arnaiz, A. Asueta, I. Robertson, Chemical depolymerisation of PET complex waste: hydrolysis vs. glycolysis, *J. Mater. Cycles Waste Manag.* 16 (2014) 201–210, <https://doi.org/10.1007/s10163-013-0177-y>.
- [12] A. Richardson, S. McPherson, J. Fasciano, R. Pauls, N. Danielson, Micellar liquid chromatography of terephthalic acid impurities, *J. Chromatogr. A* 1491 (2017) 67–74, <https://doi.org/10.1016/j.chroma.2017.02.039>.
- [13] N. Allen, M. Edge, J. Daniels, D. Royall, Spectroscopic analysis of organic contaminants in terephthalic acid: colour implications in poly (ethylene terephthalate) manufacture, *Polym. Degrad. Stab.* 62 (1998) 373–383, [https://doi.org/10.1016/S0141-3910\(98\)00024-X](https://doi.org/10.1016/S0141-3910(98)00024-X).
- [14] O. Farha, K. Mulfort, A. Thorsness, J. Hupp, Separating solids: purification of metal-organic framework materials, *J. Am. Chem. Soc.* 130 (2008) 8598–8599, <https://doi.org/10.1021/ja803097e>.
- [15] X. Chen, X. Peng, L. Jiang, X. Yuan, H. Yu, H. Wang, J. Zhang, Q. Xia, Recent advances in titanium metal-organic frameworks and their derived materials: Features, fabrication, and photocatalytic applications, *Chem. Eng. J.* 395 (2020), 125080, <https://doi.org/10.1016/j.cej.2020.125080>.
- [16] Y. Fu, D. Sun, Y. Chen, R. Huang, Z. Ding, X. Fu, Z. Li, An amine-functionalized titanium metal-organic framework photocatalyst with visible-light-induced activity for CO₂ reduction, *Angew. Chem. Int. Ed.* 51 (2012) 3364–3367, <https://doi.org/10.1002/anie.201108357>.
- [17] H. Huang, X. Wang, D. Philo, F. Ichihara, H. Song, Y. Li, D. Li, T. Qiu, S. Wang, J. Ye, Toward visible-light-assisted photocatalytic nitrogen fixation: A titanium metal organic framework with functionalized ligands, *Appl. Catal. B Environ.* 267 (2020), 118686, <https://doi.org/10.1016/j.apcatb.2020.118686>.
- [18] S. Ravichandran, V. Rajan, P. Aravind, A. Seenivasan, D. Prakash, K. Ramakrishnan, Characterization of terephthalic acid monomer recycled from

- post-consumer PET polymer bottles, *Macromol. Symp.* 361 (2016) 30–33, <https://doi.org/10.1002/masy.201400269>.
- [19] Z. Wang, X. Xie, X. Wang, A. Mahmood, H. Qiu, J. Sun, Difference of photodegradation characteristics between single and mixed VOC pollutants under simulated sunlight irradiation, *J. Photochem. Photobiol. A Chem.* 384 (2019), 112029, <https://doi.org/10.1016/j.jphotochem.2019.112029>.
- [20] M. Dan-Hardi, C. Serre, T. Frot, L. Rozes, G. Maurin, C. Sanchez, G. Férey, A new photoactive crystalline highly porous titanium(IV) dicarboxylate, *J. Am. Chem. Soc.* 131 (2009) 10857–10859, <https://doi.org/10.1021/ja903726m>.
- [21] J. Chen, X. Zhang, F. Bi, X. Zhang, Y. Yang, Y. Wang, A facile synthesis for uniform tablet-like TiO₂/C derived from Materials of Institut Lavoisier-125(Ti) (MIL-125 (Ti)) and their enhanced visible light-driven photodegradation of tetracycline, *J. Colloid Interface Sci.* 571 (2020) 275–284, <https://doi.org/10.1016/j.jcis.2020.03.055>.
- [22] R. Kaur, A. Marwaha, V. Chhabra, K. Kaushal, K. Kim, S. Tripathi, Facile synthesis of a Cu-based metal-organic framework from plastic waste and its application as a sensor for acetone, *J. Clean. Prod.* 263 (2020), 121492, <https://doi.org/10.1016/j.jclepro.2020.121492>.
- [23] Y. Xie, X. Liu, X. Ma, Y. Duan, Y. Yao, Q. Cai, Small titanium-based MOFs prepared with the introduction of tetraethyl orthosilicate and their potential for use in drug delivery, *ACS Appl. Mater. Interfaces* 10 (2018) 13325–13332, <https://doi.org/10.1021/acsami.8b01175>.
- [24] I. Ahmed, S. Jung, Effective adsorptive removal of indole from model fuel using a metal-organic framework functionalized with amino groups, *J. Hazard. Mater.* 283 (2015) 544–550, <https://doi.org/10.1016/j.jhazmat.2014.10.002>.
- [25] Z. Hasan, M. Tong, B. Jung, I. Ahmed, C. Zhong, S. Jung, Adsorption of pyridine over amino-functionalized metal-organic frameworks: Attraction via hydrogen bonding versus base-base repulsion, *J. Phys. Chem. C* 118 (2014) 21049–21056, <https://doi.org/10.1021/jp507074x>.
- [26] X. Tang, Y. Luo, Z. Zhang, W. Ding, D. Liu, J. Wang, L. Guo, M. Wen, Effects of functional groups of -NH₂ and -NO₂ on water adsorption ability of Zr-based MOFs (UiO-66), *Chem. Phys.* 543 (2021), 111093, <https://doi.org/10.1016/j.chemphys.2021.111093>.
- [27] X. Tan, J. Zhang, J. Shi, X. Cheng, D. Tan, B. Zhang, L. Liu, F. Zhang, B. Han, L. Zheng, Fabrication of NH₂-MIL-125 nanocrystals for high performance photocatalytic oxidation, *Sustain. Energy Fuels* 4 (2020) 2823–2830, <https://doi.org/10.1039/D0SE00095G>.
- [28] M. Sabo, W. Böhlmann, S. Kaskel, Titanium terephthalate (TT-1) hybrid materials with high specific surface area, *J. Mater. Chem.* 16 (2006) 2354–2357, <https://doi.org/10.1039/B601043A>.
- [29] Z. Zhu, X. He, W. Wang, Unraveling the origin of the “Turn-On” effect of Al-MIL-53-NO₂ during H₂S detection, *CrystEngComm* 22 (2020) 195–204, <https://doi.org/10.1039/C9CE01595G>.
- [30] M. Kaur, S. Mehta, S. Kansal, Amine-functionalized titanium metal-organic framework (NH₂-MIL-125(Ti)): A novel fluorescent sensor for the highly selective sensing of copper ions, *Mater. Chem. Phys.* 254 (2020), 123539, <https://doi.org/10.1016/j.matchemphys.2020.123539>.
- [31] V. Muelas-Ramos, C. Belver, J. Rodriguez, J. Bedia, Synthesis of noble metal-decorated NH₂-MIL-125 titanium MOF for the photocatalytic degradation of acetaminophen under solar irradiation, *Sep. Purif. Technol.* 272 (2021), 118896, <https://doi.org/10.1016/j.seppur.2021.118896>.
- [32] H. Wang, X. Zhang, F. Zheng, Y. Huang, Q. Li, Surfactant effect on synthesis of core-shell LiFePO₄/C cathode materials for lithium-ion batteries, *J. Solid State Electrochem.* 19 (2015) 187–194, <https://doi.org/10.1007/s10008-014-2598-5>.
- [33] R. Hailili, Z. Wang, X. Gong, C. Wang, Octahedral-shaped perovskite CaCu₃Ti₄O₁₂ with dual defects and coexposed {001}, {111} facets for visible-light photocatalysis, *Appl. Catal. B Environ.* 254 (2019) 86–97, <https://doi.org/10.1016/j.apcatb.2019.03.086>.
- [34] S. Kim, J. Kim, H. Kim, H. Cho, W. Ahn, Adsorption/catalytic properties of MIL-125 and NH₂-MIL-125, *Catal. Today* 204 (2013) 85–93, <https://doi.org/10.1016/j.cattod.2012.08.014>.
- [35] H. Wang, X. Yuan, Y. Wu, G. Zeng, X. Chen, L. Leng, Z. Wu, L. Jiang, H. Li, Facile synthesis of amino-functionalized titanium metal-organic frameworks and their superior visible-light photocatalytic activity for Cr(VI) reduction, *J. Hazard. Mater.* 286 (2015) 187–194, <https://doi.org/10.1016/j.jhazmat.2014.11.039>.
- [36] Q. Hu, S. Yin, Y. Chen, B. Wang, M. Li, Y. Ding, J. Di, J. Xia, H. Li, Construction of MIL-125(Ti)/ZnIn₂S₄ composites with accelerated interfacial charge transfer for boosting visible light photoreactivity, *Colloids Surf. A Physicochem. Eng. Asp.* 585 (2020), 124078, <https://doi.org/10.1016/j.colsurfa.2019.124078>.
- [37] K. An, H. Ren, D. Yang, Z. Zhao, Y. Gao, Y. Chen, J. Tan, W. Wang, Z. Jiang, Nitrogenase-inspired bimetallic metal organic frameworks for visible-light-driven nitrogen fixation, *Appl. Catal. B Environ.* 292 (2021), 120167, <https://doi.org/10.1016/j.apcatb.2021.120167>.
- [38] B. Liu, Y. Zhan, R. Xie, H. Huang, K. Li, Y. Zeng, R. Shrestha, Efficient photocatalytic oxidation of gaseous toluene in a bubbling reactor of water, *Chemosphere* 233 (2019) 754–761, <https://doi.org/10.1016/j.chemosphere.2019.06.002>.
- [39] H. Liu, F. Wang, K. Hu, T. Li, Y. Yan, J. Li, The adsorption and sensing performances of ir-modified MoS₂ monolayer toward SF₆ decomposition products: A DFT study, *Nanomaterials* 11 (2021) 100, <https://doi.org/10.3390/nano11010100>.
- [40] S. Subudhi, K. Parida, Zr-based MOF: an enhanced photocatalytic application towards H₂ evolution by consequence of functional group and LSPR effect, *Mater. Today Proc.* 35 (2021) 198–202, <https://doi.org/10.1016/j.matpr.2020.04.252>.
- [41] A. González, M. Sierra, A. Almansa, F. Sánchez, M. Iglesias, Amino-functionalized zirconium and cerium MOFs: Catalysts for visible light induced aerobic oxidation of benzylic alcohols and microwaves assisted N-Alkylation of amines, *Appl. Catal. A Gen.* 623 (2021), 118287, <https://doi.org/10.1016/j.apcata.2021.118287>.
- [42] M. Salimi, A. Esrafil, A. Jonidi Jafari, M. Gholami, H. Sobhi, M. Nourbakhsh, B. Adergani, Photocatalytic degradation of cefixime with MIL-125(Ti)-mixed linker decorated by g-C₃N₄ under solar driven light irradiation, *Colloids Surf. A Physicochem. Eng. Asp.* 582 (2019), 123874, <https://doi.org/10.1016/j.colsurfa.2019.123874>.
- [43] J. Wang, A. Cherevan, C. Hannecart, S. Naghdi, S. Nandan, T. Gupta, D. Eder, Ti-based MOFs: New insights on the impact of ligand composition and hole scavengers on stability, charge separation and photocatalytic hydrogen evolution, *Appl. Catal. B Environ.* 283 (2021), 119626, <https://doi.org/10.1016/j.apcatb.2020.119626>.
- [44] G. Capano, F. Ambrosio, S. Kampouri, K. Stylianou, A. Pasquarello, B. Smit, On the electronic and optical properties of metal-organic frameworks: case study of MIL-125 and MIL-125-NH₂, *J. Phys. Chem. C* 124 (2020) 4065–4072, <https://doi.org/10.1021/acs.jpcc.9b09453>.
- [45] Z. Zhang, L. Huang, S. Sheng, C. Jiang, Y. Wang, MIL-125(Ti)-derived COOH functionalized TiO₂ grafted molecularly imprinted polymers for photoelectrochemical sensing of ofloxacin, *Sens. Actuators B Chem.* 343 (2021), 130119, <https://doi.org/10.1016/j.snb.2021.130119>.
- [46] X. Zhang, J. Chen, S. Jiang, X. Zhang, F. Bi, Y. Yang, Y. Wang, Z. Wang, Enhanced photocatalytic degradation of gaseous toluene and liquid tetracycline by anatase/rutile titanium dioxide with heterophase junction derived from materials of institut lavoisier-125(Ti): Degradation pathway and mechanism studies, *J. Colloid Interface Sci.* 588 (2021) 122–137, <https://doi.org/10.1016/j.jcis.2020.12.042>.
- [47] P.V. Hlophe, L.C. Mahlalela, L.N. Dlamini, A composite of platelet-like orientated BiVO₄ fused with MIL-125(Ti): Synthesis and characterization, *Sci. Rep.* 9 (2019) 10044, <https://doi.org/10.1038/s41598-019-46498-w>.
- [48] C. Liu, T. Bao, L. Yuan, C. Zhang, J. Wang, J. Wan, C. Yu, Semiconducting MOF@ZnS heterostructures for photocatalytic hydrogen peroxide production: Heterojunction coverage matters, *Adv. Funct. Mater.* (2021), 2111404, <https://doi.org/10.1002/adfm.202111404>.
- [49] S. Wang, Z. Li, Y. Guan, L. Lu, Z. Shi, P. Weng, S. Yan, Z. Zou, Visible light driven TaON/V₂O₅ heterojunction photocatalyst for deep elimination of volatile-aromatic compounds, *Appl. Catal. B Environ.* 245 (2019) 220–226, <https://doi.org/10.1016/j.apcatb.2018.12.067>.
- [50] Q. Zhou, Q. Zhao, W. Xiong, X. Li, J. Li, L. Zeng, Hollow porous zinc cobaltate nanocubes photocatalyst derived from bimetallic zeolitic imidazolate frameworks towards enhanced gaseous toluene degradation, *J. Colloid Interface Sci.* 516 (2018) 76–85, <https://doi.org/10.1016/j.jcis.2018.01.042>.
- [51] H. Mehrizadeh, A. Niaei, H. Tseng, D. Salari, A. Khataee, Synthesis of ZnFe₂O₄ nanoparticles for photocatalytic removal of toluene from gas phase in the annular reactor, *J. Photochem. Photobiol. A Chem.* 332 (2017) 188–195, <https://doi.org/10.1016/j.jphotochem.2016.08.028>.
- [52] X. Huang, D. Wang, Q. Yang, Y. Peng, J. Li, Multi-pollutant control (MPC) of NO and chlorobenzene from industrial furnaces using a vanadia-based SCR catalyst, *Appl. Catal. B Environ.* 285 (2021), 119835, <https://doi.org/10.1016/j.apcatb.2020.119835>.
- [53] P. Kumari, B. Rao, D. Mallesh, N. Lingaiah, Niobium exchanged tungstophosphoric acid supported on titania catalysts for selective synthesis of 5-ethoxymethylfurfural from fructose, *Mol. Catal.* 508 (2021), 111607, <https://doi.org/10.1016/j.mcat.2021.111607>.
- [54] L. Yang, H. Zhang, P. Tao, X. Lu, X. Li, C. Wang, B. Wang, F. Yue, D. Zhou, Q. Xia, Microwave-assisted air epoxidation of mixed biolefins over a spherical bimetal ZnCo-MOF catalyst, *ACS Appl. Mater. Interfaces* 13 (2021) 8474–8487, <https://doi.org/10.1021/acsami.0c22317>.
- [55] F. Vermoortele, B. Bueken, G. Bars, B. Voorde, M. Vandichel, K. Houthoofd, A. Vimont, M. Daturi, M. Waroquier, V. Speybroeck, C. Kirschhock, D. Vos, Synthesis modulation as a tool to increase the catalytic activity of metal-organic frameworks: the unique case of UiO-66(Zr), *J. Am. Chem. Soc.* 135 (2013) 11465–11468, <https://doi.org/10.1021/ja405078u>.
- [56] J. Hajek, B. Bueken, M. Waroquier, D. Vos, V. Speybroeck, The remarkable amphoteric nature of defective UiO-66 in catalytic reactions, *ChemCatChem* 9 (2017) 2203–2210, <https://doi.org/10.1002/cctc.201601689>.
- [57] H. Leclerc, A. Vimont, J. Lavalley, M. Daturi, A. Wiersum, P. Llwelllyn, P. Horcajada, G. Férey, C. Serre, Infrared study of the influence of reducible iron (iii) metal sites on the adsorption of CO, CO₂, propane, propene and propyne in the mesoporous metal-organic framework MIL-100, *Phys. Chem. Chem. Phys.* 13 (2011) 11748–11756, <https://doi.org/10.1039/C1CP20502A>.
- [58] Y. Xu, Z. Wang, H. Tan, K. Jing, Z. Xu, G. Guo, Lewis acid sites in MOFs supports promoting the catalytic activity and selectivity for CO esterification to dimethyl carbonate, *Catal. Sci. Technol.* 10 (2020) 1699–1707, <https://doi.org/10.1039/C9CY02330E>.
- [59] J. Lyu, L. Sun, Q. Fu, M. Zhang, J. Gao, J. Li, Enhancement of photocatalytic mineralization efficiency of toluene by inducing TiO₂-homogenous-adsorption-layer, *Chin. J. Environ. Eng.* 11 (2017) 3691–3696.
- [60] S. Du, Q. Sun, N. Wang, X. Chen, M. Jia, J. Yu, Synthesis of hierarchical TS-1 zeolites with abundant and uniform intracrystalline mesopores and their highly efficient catalytic performance for oxidation desulfurization, *J. Mater. Chem. A* 5 (2017) 7992–7998, <https://doi.org/10.1039/C6TA10044A>.
- [61] M. Chen, X. Wei, L. Zhao, Y. Huang, S. Lee, W. Ho, K. Chen, Novel N/carbon quantum dot modified MIL-125(Ti) composite for enhanced visible-light photocatalytic removal of NO, *Ind. Eng. Chem. Res.* 59 (2020) 6470–6478, <https://doi.org/10.1021/acs.iecr.9b06816>.
- [62] M. Chen, C. Guo, S. Hou, J. Lv, Y. Zhang, H. Zhang, J. Xu, A novel Z-scheme AgBr/P-g-C₃N₄ heterojunction photocatalyst: excellent photocatalytic performance and

- photocatalytic mechanism for ephedrine degradation, *Appl. Catal. B Environ.* 266 (2020), 118614, <https://doi.org/10.1016/j.apcatb.2020.118614>.
- [63] Z. Rao, G. Lu, L. Chen, A. Mahmood, G. Shi, Z. Tang, X. Xie, J. Sun, Photocatalytic oxidation mechanism of Gas-Phase VOCs: unveiling the role of holes, OH and $O_2^{\cdot-}$, *Chem. Eng. J.* 430 (2022), 132766, <https://doi.org/10.1016/j.cej.2021.132766>.
- [64] Y. Liang, J. Li, Y. He, Z. Jiang, W. Shangguan, Catalytic oxidation of dimethyl phthalate over titania-supported noble metal catalysts, *J. Hazard. Mater.* 401 (2021), 123274, <https://doi.org/10.1016/j.jhazmat.2020.123274>.
- [65] Z. Rao, G. Lu, A. Mahmood, G. Shi, X. Xie, J. Sun, Deactivation and activation mechanism of TiO_2 and $rGO/Er^{3+}-TiO_2$ during flowing gaseous VOCs photodegradation, *Appl. Catal. B Environ.* 284 (2021), 119813, <https://doi.org/10.1016/j.apcatb.2020.119813>.
- [66] X. Li, J. Li, Y. Shi, M. Zhang, S. Fan, Z. Yin, M. Qin, T. Lian, X. Li, Rational design of cobalt and nitrogen co-doped carbon hollow frameworks for efficient photocatalytic degradation of gaseous toluene, *J. Colloid Interface Sci.* 528 (2018) 45–52, <https://doi.org/10.1016/j.jcis.2018.05.067>.
- [67] J. Zhong, Y. Zeng, D. Chen, S. Mo, M. Zhang, M. Fu, J. Wu, Z. Su, P. Chen, D. Ye, Toluene oxidation over Co^{3+} -rich spinel Co_3O_4 : Evaluation of chemical and by-product species identified by in situ DRIFTS combined with PTR-TOF-MS, *J. Hazard. Mater.* 386 (2020), 121957, <https://doi.org/10.1016/j.jhazmat.2019.121957>.
- [68] Z. Yin, B. Liu, S. Fan, P. Wang, X. Wang, D. Long, L. Zhang, X. Yang, X. Li, In situ FTIR spectra investigation of the photocatalytic degradation of gaseous toluene over a novel hedgehog-like $CaFe_2O_4$ hollow-structured materials, *Catal. Commun.* 130 (2019), 105754, <https://doi.org/10.1016/j.catcom.2019.105754>.
- [69] X. Yang, X. Yu, M. Jing, W. Song, J. Liu, M. Ge, Defective $Mn_xZr_{1-x}O_2$ solid solution for the catalytic oxidation of toluene: insights into the oxygen vacancy contribution, *ACS Appl. Mater. Interfaces* 11 (2019) 730–739, <https://doi.org/10.1021/acsami.8b17062>.
- [70] M. Huang, S. Wang, L. Li, H. Zhang, Z. Shi, Y. Chen, Effect of high temperature pretreatment on the thermal resistance properties of $Pd/CeO_2/Al_2O_3$ close-coupled catalysts, *J. Rare Earths* 35 (2017) 149–157, [https://doi.org/10.1016/S1002-0721\(17\)60893-7](https://doi.org/10.1016/S1002-0721(17)60893-7).
- [71] S. Ali, M. Humayun, W. Pi, Y. Yuan, M. Wang, A. Khan, P. Yue, L. Shu, Z. Zheng, Q. Fu, W. Luo, Fabrication of $BiFeO_3-g-C_3N_4-WO_3$ Z-scheme heterojunction as highly efficient visible-light photocatalyst for water reduction and 2,4-dichlorophenol degradation: Insight mechanism, *J. Hazard. Mater.* 397 (2020), 122708, <https://doi.org/10.1016/j.jhazmat.2021.126772>.
- [72] W. Yang, Z. Su, Z. Xu, W. Yang, Y. Peng, J. Li, Comparative study of α -, β -, γ - and δ - MnO_2 on toluene oxidation: Oxygen vacancies and reaction intermediates, *Appl. Catal. B Environ.* 260 (2020), 118150, <https://doi.org/10.1016/j.apcatb.2019.118150>.
- [73] R. Chen, J. Li, J. Sheng, W. Cui, X. Dong, P. Chen, H. Wang, Y. Sun, F. Dong, Unveiling the unconventional roles of methyl number on the ring-opening barrier in photocatalytic decomposition of benzene, toluene and o-xylene, *Appl. Catal. B Environ.* 278 (2020), 119318, <https://doi.org/10.1016/j.apcatb.2020.119318>.
- [74] G. Li, L. Wang, C. Wen, F. Li, P. Wu, B. Wang, K. Shen, Y. Zhang, S. Zhang, R. Xiao, Deep insight into the catalytic removal mechanism of a multi-active center catalyst for chlorobenzene: an experiment and density functional theory study, *Catal. Sci. Technol.* 10 (2020) 6879–6891, <https://doi.org/10.1039/D0CY01372B>.
- [75] L. Liu, B. Zhou, Y. Liu, J. Liu, L. Hu, Y. Tang, M. Wang, In-situ regulation of acid sites on Mn-based perovskite@mullite composite for promoting catalytic oxidation of chlorobenzene, *J. Colloid Interface Sci.* 606 (2021) 1866–1873, <https://doi.org/10.1016/j.jcis.2021.08.145>.